

COPYRIGHT WARNING

This paper is protected by copyright. You are advised to print or download **ONE COPY** of this paper for your own private reference, study and research purposes. You are prohibited having acts infringing upon copyright as stipulated in Laws and Regulations of Intellectual Property, including, but not limited to, appropriating, impersonating, publishing, distributing, modifying, altering, mutilating, distorting, reproducing, duplicating, displaying, communicating, disseminating, making derivative work, commercializing and converting to other forms the paper and/or any part of the paper. The acts could be done in actual life and/or via communication networks and by digital means without permission of copyright holders.

The users shall acknowledge and strictly respect to the copyright. The recitation must be reasonable and properly. If the users do not agree to all of these terms, do not use this paper. The users shall be responsible for legal issues if they make any copyright infringements. Failure to comply with this warning may expose you to:

- Disciplinary action by the Vietnamese-German University.
- Legal action for copyright infringement.
- Heavy legal penalties and consequences shall be applied by the competent authorities.

The Vietnamese-German University and the authors reserve all their intellectual property rights.



SCALING A HIGH-PRESSURE ZERO-GAP ELECTROLYZER FOR CONTINUOUS CO₂ REDUCTION

Ngô Thanh Nguyễn

Matriculation number: 108020266369



Vietnamese-German University

BACHELOR THESIS

Degree: Mechanical Engineering

Faculty of Mechanical Engineering

Ruhr Universität Bochum and Vietnamese German University

Submitted date: 13th November 2023

Examiner: Prof. apl. Dr.-Ing. A. Kilzer

Prof. Dr. Ulf-Peter Apfel

Supervisor: MSc. Stephan Heuser

Dr.-Ing. Lucas Hoof

Conducted at the research institute Fraunhofer UMSICHT.

Preface

This bachelor thesis topic “Scaling a high-pressure zero-gap electrolyzer for continuous CO₂ reduction” includes the technical numbers and information from researches at Ruhr Universität Bochum and the Fraunhofer Institute for Environmental, Safety, and Energy Technology UMSICHT.

This thesis would be only viewed by supervisors, examiners and the authorized members. Any publication, reproduction and inspection of the third parties for this thesis needs to get the permission from Ruhr Universität Bochum, Fraunhofer UMSICHT as well as Vietnamese German University.

Without the available permission, publication and reproduction are not allowed under any circumstances.



Formula symbols

Symbol	Definition	Unit
a_p	Depth of milling cutter for one cut	mm
$A_{existing}$	Existing electrode area	mm ²
$A_{inlet/outlet}$	Area of CO ₂ inlet or outlet	mm ²
A_{last}	Loaded cross section area	mm ²
A_{new}	New electrode area	mm ²
A_p	Head surface area	mm ²
A_s	Load cross section	mm ²
A_{water}	Area of water inlet or outlet	mm ²
b_4	Width of the O-ting installation space	mm
c_5	Design allowance	mm
C_{HD}	Pitch diameter	mm
d_1	Inner diameter of the O-ring	mm
d_2	Core size diameter	mm
d_3	Core diameter of screw	mm
d_7	Outer diameter of the installation space with sealing	mm
d_8	Inner diameter of the installation space with sealing	mm
d_b	Diameter of screw	mm
$d_{inlet/outlet}$	Diameter of the CO ₂ inlet or outlet	mm
$d_{k_{BZ}}$	Thread core diameter construction	mm
d_{last}	Loaded diameter	mm
d_{mill}	Diameter of the milling cutter	mm
d_{washer}	Diameter of washer	mm
d_{water}	Diameter of water inlet or outlet	mm
D	Diameter of the nut	mm
D_1	Diameter of connection tools to the hexagon socket	mm
D_2	Outer diameter of the hexagon socket	mm
$D_{a_{components}}$	Outer diameter of the components	mm
$D_{i_{components}}$	Inner diameter of the components	mm
e	Minimum thickness of the end plate	mm
e_A	Minimum thickness of the end plate for installed condition	mm
$e_{components}$	Radial wall thickness of the components	mm
$e_{copper\ plate}$	Radial wall thickness of the copper plate	mm
$e_{flow\ field}$	Radial wall thickness of the flow field	mm
e_{nut}	Height of the hexagon nut	mm

e_{p_1}	Minimum thickness of the end plate for operating condition	mm
E	Young modulus	MPa
f	Internal stress of material at temperature	MPa
f_A	Internal stress of material at room temperature	MPa
f_z	Set amount	μm
$f_{z_{\text{head/nut support}}}$	Set amount of head or nut support	μm
$f_{z_{\text{inner parting line}}}$	Set amount of inner parting line	μm
$f_{z,p}$	Feed per tooth for the plunge milling	mm
$f_{z,s}$	Feed per tooth for the slot milling	mm
$f_{z_{\text{thread}}}$	Set amount of thread	μm
F_B	Operating force	kN
F_{KL}	Clamping force	kN
F_{DB}	Operating sealing force	N
F_{FB}	Minimum bolt force element	N
F_{RB}	Minimum bolt force element	N
F_{SB}	Bolt force for operating condition	N
F_{Sp}	Tightening force	kN
G_0	Mean seal diameter	mm
h	Depth of the O-ring installation space	mm
κ	Reduction factor	-
k_{1FL}	Characteristic value	-
k_A	Dressing factor	-
k_{M16}	Yield strength	MPa
l_k	Clamping length	mm
L	Total length of the hexagon socket	mm
L_1	Length of the head of the connection tools	mm
\dot{m}_{exist}	Mass flow of CO ₂ at existing reactor	kg h ⁻¹
m_{nut}	Thickness of the hexagon nut	mm
$\dot{m}_{\text{scale-up}}$	Mass flow of CO ₂ at scale-up reactor	kg h ⁻¹
M_{sp}	Tightening moment	Nm
$n_{\text{compartment}}$	Number of compartments	compartments
$n_{\text{components}}$	Number of components	components
n_{screw}	Number of screws	Screws
p	Operating pressure	bar
p_{zul}	Operating pressure	bar
P_{FP}	Pressure surface	MPa

Re	Reynold number	-
$R_{m/T}$	Tensile strength of material at temperature	MPa
$R_{m/RT}$	Tensile strength of material at room temperature	MPa
$R_{p1,0/T}$	1% yield strength of material	MPa
R_z	Roughness	μm
s_{nut}	Width of the hexagon nut	mm
S_0	Safety factor	-
t_b	The mean pitch	mm
v	Velocity of CO ₂ flow	mm s^{-1}
v_c	Velocity of the milling cutter	m min^{-1}
v_{water}	Velocity of water flow	mm s^{-1}
\dot{V}_{exist}	Volume flow of water at existing reactor	l s^{-1}
$\dot{V}_{scale-up}$	Volume flow of water at the scale-up reactor	l s^{-1}
w_A	Designed bolt load	N
y_0	Minimum surface pressure	MPa
y_1	Lever arm measured from the outer edge of the end plate to the center of the wall thickness of the container	mm
y_2	Lever arm measured from the outer edge of the end plate to the bolt pitch diameter	mm
y_{GRD}		MPa
z_{BZ}	Auxiliary quality	-
β	Compliance factor	-
ρ	Density	kg m^{-3}
μ	Dynamic viscosity	Pa.s
μ_{EP}	Auxiliary value	-
μ_G	Static friction	-
μ_k	Kinetic friction	-

List of figures

Figure 1. A schematic diagram of circular production from CO ₂ electrolyzer [3].	1
Figure 2. Schematic structures of an H-cell electrolyzer [5].	3
Figure 3. The Schematic architecture of a continuous reactor for CO ₂ reduction [2].	4
Figure 4. Membrane-based reactor with an MEA featuring anode and cathode gas diffusion electrodes [11].	5
Figure 5. A simple structure of a gas diffusion electrode (GDE) [16].	6
Figure 6. Types of different membranes [18].	7
Figure 7. Stack components according to [2].	7
Figure 8. Common types of fluid flow channels a/ Serpentine fluid flow channels, b/ Parallel fluid flow channels, c/ Interdigitated fluid flow channels [20]	8
Figure 9. A zero-gap electrolyzer schematic according to [25].	9
Figure 10. Configuration of the high-pressure electrolyzer at Fraunhofer UMSICHT.	10
Figure 11. The O-ring gasket characteristic [26].	15
Figure 12. Cross-section of the nut design [42].	27
Figure 13. CAD M16 hex nut.	27
Figure 14. Cross-section of the hexagon socket design [43].	27
Figure 15. Diameter of the milling cutter.	28
Figure 16. The depth of the milling cutter for one cut.	28
Figure 17. Front view of anode flow field design.	30
Figure 18. Back view of the anode flow field design.	30
Figure 19. Dimensions of the anode flow field.	31
Figure 20. Front view of the cathode flow field design.	32
Figure 21. Back view of the cathode flow field design.	32
Figure 22. Dimension of the cathode flow field.	32
Figure 23. End plate at the last cathode flow field side.	33
Figure 24. End plate at the last anode flow field side.	33
Figure 25. Pin centering.	33
Figure 26. Exploded view of one stack.	34
Figure 27. The last stack with different anode flow field.	34
Figure 28. The cell assembly design.	35
Figure 29. Exploded view of the cell assembly.	35

List of tables

Table 1. Overview information about the existing plates used in zero-gap reactors.....	10
Table 2. Selection of electrode diameter.	11
Table 3. Comparison between the existing reactor and the aim for the scale-up one.	12
Table 4. The technical data when using slot milling cutter for titanium workpieces [44].	29



List of equations

Equation 1. New electrode areas for scale-up reactor.....	11
Equation 2. The thread core diameter construction of the end plate.....	13
Equation 3. Condition for design allowance determination [26].....	13
Equation 4. Auxiliary quality.....	13
Equation 5. The bolt force for operating conditions based on [26].....	14
Equation 6. Minimum bolt force element based on [26].....	14
Equation 7. Minimum bolt force element based on [26].....	14
Equation 8. Operating sealing force based on [26].....	14
Equation 9. The bolt force for operating condition.....	14
Equation 10. Shortened bolt force for operation condition.....	14
Equation 11. Mean seal diameter.....	14
Equation 12. Lever arm ratio.....	15
Equation 13. The bolt force for operating condition.....	15
Equation 14. Minimum number of screws [26,33].....	15
Equation 15. Minimum diameter of the end plate.....	15
Equation 16. Auxiliary quality [26].....	16
Equation 17. Condition for design allowance determination.....	16
Equation 18. The thread core diameter construction of the end plate.....	16
Equation 19. The minimum thickness of the end plate for the installed condition [27].....	16
Equation 20. The bolt load for the installed condition [27].....	16
Equation 21. Internal stress of the material.....	17
Equation 22. The internal stress of the material.....	17
Equation 23. The mean pitch of screws.....	17
Equation 24. The mean pitch of screws.....	17
Equation 25. The minimum thickness of the end plate.....	17
Equation 26. The minimum thickness of the end plate with operation condition [27].....	17
Equation 27. Designed bolt load for the assembled condition [27].....	18
Equation 28. The minimum thickness for the installed condition [27].....	18
Equation 29. The minimum thickness of the end plate with operation condition [27].....	18
Equation 30. The internal stress of the material at room temperature.....	18
Equation 31. The minimum thickness of the end plate with operation condition.....	18
Equation 32. The minimum thickness of the end plate.....	19
Equation 33. The outer diameter of the components.....	19
Equation 34. The radial wall thickness of the components.....	19
Equation 35. The radial wall thickness based on [27].....	19
Equation 36. The internal stress of the titanium material.....	19
Equation 37. The radial wall thickness of the flow field.....	19
Equation 38. The internal stress of the copper material.....	20
Equation 39. The radial wall thickness of the copper plate.....	20
Equation 40. The radial wall thickness of the components.....	20
Equation 41. The outer diameter of the components.....	20
Equation 42. The require stress cross section.....	20

Equation 43. The operating force for the screws.....	20
Equation 44. The pressure surface of the screws [30].....	21
Equation 45. Clamping length.	21
Equation 46. The total set amount [30].....	21
Equation 47. The set amount of head or nut support.	21
Equation 48. The set amount of the inner parting line.	21
Equation 49. The total set amount.....	22
Equation 50. The loaded cross-section area.....	22
Equation 51. The operating force for the screws.....	22
Equation 52. The operating pressure.	22
Equation 53. Reynolds number [41].....	24
Equation 54. Mass flow for the scale-up reactor.	24
Equation 55. Velocity of the flow [41].....	24
Equation 56. Area of the inlet and outlet of CO₂ flow.....	24
Equation 57. Volume flow of water for scale-up reactor.....	25
Equation 58. Volume flow of water per compartment.	25
Equation 59. The water inlet and outlet area.	25
Equation 60. Velocity of water flow.	25
Equation 61. Comparison between the mean pitch of the screws and the outer diameter.	28
Equation 62. Depth of the cut.	29



Vietnamese-German University

Table of Contents

Preface.....	ii
Formula symbols.....	iii
List of figures.....	vi
List of tables.....	vii
1. Introduction.....	1
2. Theoretical fundamentals.....	3
2.1. Electrolysis in an H-cell.....	3
2.2. Continuous CO ₂ electrolysis reactor architecture.....	4
2.3. Zero-gap reactor architecture.....	4
2.3.1. Membrane electrode assembly.....	5
2.3.2. Gas diffusion electrodes.....	5
2.3.3. Gas diffusion layer.....	6
2.3.4. Catalyst layer.....	6
2.3.5. Membrane.....	6
2.4. Other components.....	7
3. State of the Art.....	9
3.1. CO ₂ reduction in MEA-type Electrolyzers.....	9
3.2. Continuous PEM electrolyzer at Fraunhofer UMSICHT.....	9
4. Objective.....	11
5. Stress calculation of the zero-gap reactor.....	13
5.1. Tightness of the sealing according to AD2000.....	13
5.2. Calculation of axial wall thickness of the end plate.....	16
5.3. Calculation of the radial wall thickness of the components.....	19
5.4. Screw strength calculation according to Roloff/Matek.....	20
5.5. Calculation of pins.....	22
6. Calculation of fluid channels.....	23
6.1. O-ring selections for electrode flow field.....	23
6.2. Scaling parameter of CO ₂ stream.....	23
6.3. Scaling parameter of water stream.....	25
7. Additional parameters.....	27
7.1. Screws and nuts.....	27
7.2. Milling tools.....	28

8. 3D CAD models of reactor component.....	30
8.1. Anode flow field.....	30
8.2. Cathode flow field	31
8.3. End plate.....	33
8.4. Overview	34
9. Conclusion and outlook	36
References.....	37
Appendix.....	39



1. Introduction

With the increasing population and the demand for vehicles, the amount of greenhouse that is released directly into the air is increasing. This is one of the reasons that cause climate change and environmental pollution. In 2022, more than 321 million tons of CO₂ were emitted into the atmosphere than the previous year, setting a new record for CO₂ emissions at over 36.8 Gt of CO₂ [1]. Researchers are investigating suitable solutions to improve environmental situations such as producing transportation fuels and chemicals. The conversion of CO₂ is used as one of the methods for obtaining renewable energy [2].

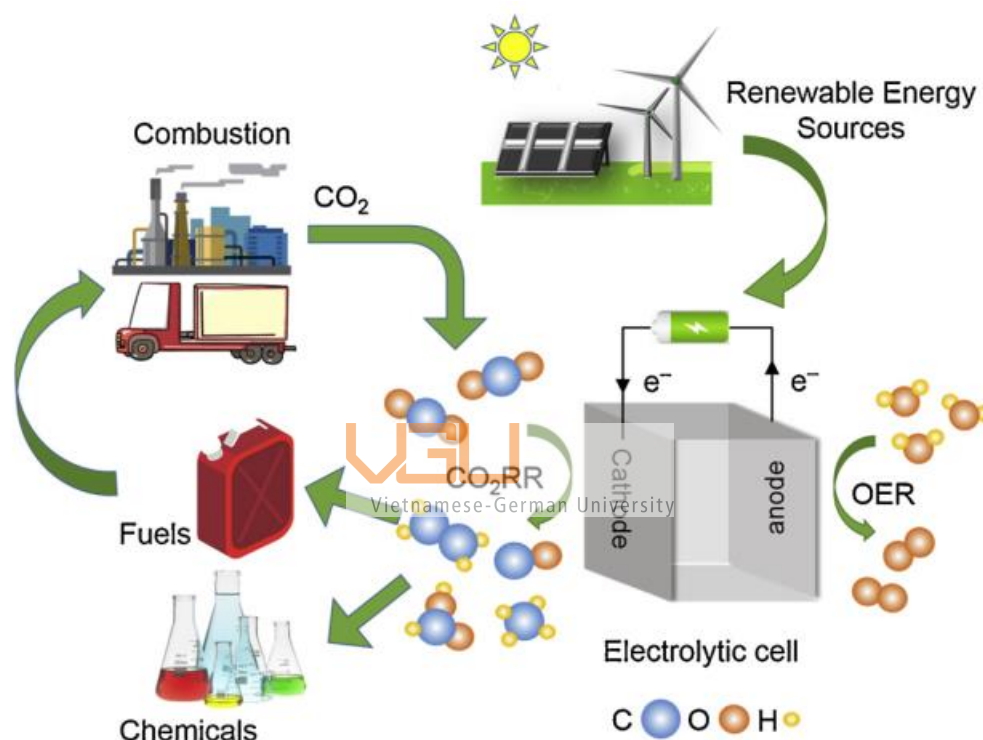


Figure 1. A schematic diagram of circular production from CO₂ electrolyzer [3].

In the renewable energy industry, there is increasing interest in CO₂ reduction reactors, especially the polymer-electrolyte membrane (PEM) based water electrolyzer technology [4]. This type of continuous reactor is now existing and investigated at Fraunhofer UMSICHT.

The existing reactor at Fraunhofer UMSICHT contains one stack, which means the electrodes are in contact directly with an ion exchange membrane and separated by anode and cathode electrocatalysts. CO₂ flow is supplied through the cathode while the fluid is flowing along the anode. The reactor can be worked under 200 bar(g) of pressure condition and 36 g h⁻¹ of CO₂ mass flow. Additionally, the area of an electrode is 12.6 cm².

With the increasing CO₂ mass flow, the relevant size of the reactor cannot be put into the renewable energy industry due to its low workload. Scaling up the existing electrolyzer is a possible solution

to recycle the CO₂ that is put into the environment as well as produce more products from the circulation. To achieve this goal, the scale-up technology for a continuous-flow reactor is used. The scale-up is first designed by increasing the mass flow of CO₂ [2] to 1 kg h⁻¹ while maintaining the working pressure in order to test the suitability of the method.

In addition, the centering method is changing from the existing design, which uses screws to fix the compartments. The operating pressure of the new centering method should be calculated to check whether it will adapt to the working condition of the electrolyzer. The calculations of Reynolds numbers and pressure drop are also included to certain the flow properties and the possibilities due to working conditions.

Overall, the ongoing research development efforts focus on advancing the capabilities of continuous-flow electro-reduction of CO₂ by PEM-based water technology as a reducing CO₂ emission solution. Scaling up and optimizing the reactor system due to the structural design and operational parameters to reach higher expectations.



2. Theoretical fundamentals

2.1. Electrolysis in an H-cell

Currently, an H-cell type is the most common one that is used in laboratories as a CO₂ reduction reactor. A typical “H” form cell consists of an anodic and a cathodic compartment separated by an ion-exchange membrane and connected through the circular chamber. These components are constructed to prevent the reduction of the products from oxidizing during the reaction. **Figure 2** illustrates a schematic diagram of the conventional H-type electrochemical cell. This configuration is based on three electrodes connected to the potentiostat: working electrodes (WE), reference electrode (RE), and counter electrode (CE) [3].

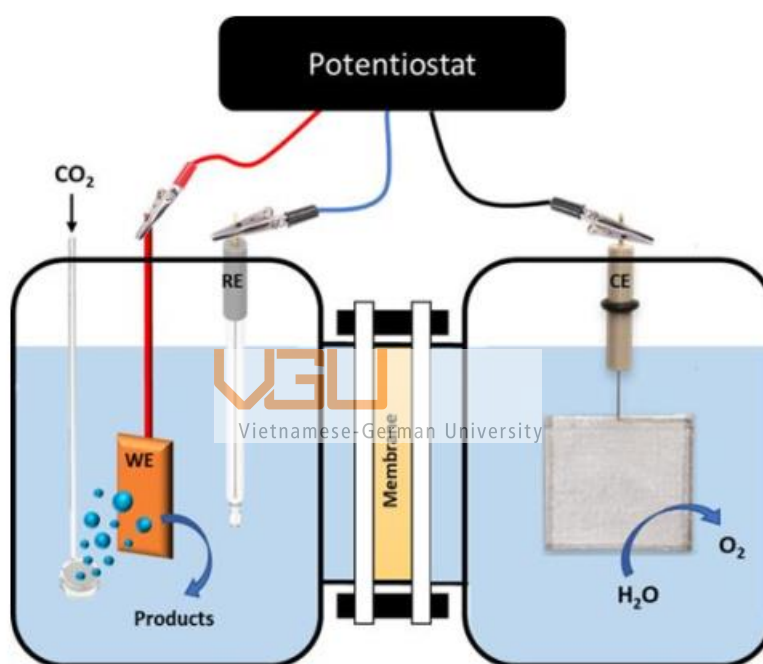


Figure 2. Schematic structures of an H-cell electrolyzer [5].

The WE and RE are set in the cathodic compartment, and the CE is located in the anodic one. These compartments are also known as sections or chambers. In addition, the sections are separated by an ion-exchange membrane in order to avoid the reduction of products due to reoxidation. The cathodic chamber is connected directly to the CO₂ through a tube or a glass frit [5]. Electrons, protons, and O₂ are produced when the oxidation of water occurs after applying a voltage at the anode side [6]. The external circuit at the anodic compartment transfers the electrons while the protons are carried out across the proton-exchange membrane and consumed at the cathodic compartment [7]. As a result of the transportation, the reactants reduce at the cathode during the consumption of electrons and protons. In addition, the protons also can be reduced by the electrons making hydrogen (H₂) arise. This process is known as hydrogen evolutionary reaction (HER) [8].

2.2. Continuous CO₂ electrolysis reactor architecture

A continuous CO₂ electrolysis reactor is a type of H-cell batch reactor. It is used to convert CO₂ into CO, formic acid, and other chemicals during the electrochemical process [2]. This design can achieve high energy efficiency, working in high operating conditions, and can be easily scaled up for industrial applications [9].

The structure shown in **figure 3** is the most popular structure that is used for the continuous flow cell. The configuration consists of an anodic flow channel and a cathodic flow channel, which are separated by an ion-exchange membrane. Other configurations can be derived from this setup. The anolyte and catholyte are fed through a channel between the gas diffusion electrodes (GDE) and the membrane [2]. In the high-pressure CO₂ electrolyzer, which is also called a zero-gap design, the gas diffusion electrodes (GDE) are contacted directly to the membrane. The reactants are guided by the plate with flow channels, known as the “flow field”, in both the anode and cathode side [10].

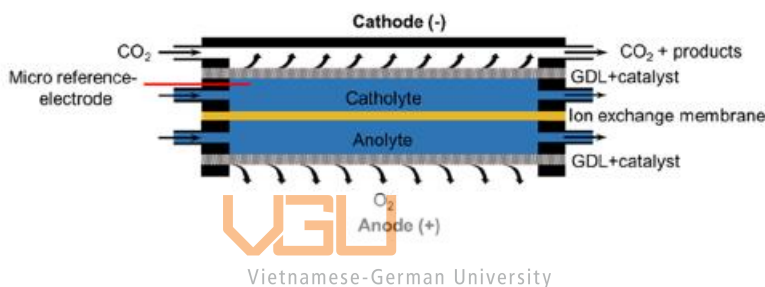


Figure 3. The Schematic architecture of a continuous reactor for CO₂ reduction [2].

2.3. Zero-gap reactor architecture

The construction of the zero-gap electrolyzer is shown in this section. A polymer electrolyte membrane (PEM) electrolyzer is also known as a membrane electrode assembly (MEA) electrolyzer [5]. Compared to the batch reactors, the PEM electrolyzer can operate at higher current densities, higher temperatures as well as higher efficiency [9]. These benefits not only prevent the oxidization of CO₂ reduction products but also simplify the design of the reactor by requiring fewer components. In addition, it also works under higher pressures between the electrodes when the cross-over of reactants is suppressed [5]. In any reactor with a membrane, the separation between the anode and cathode side by the ion-exchange membrane can avoid the reoxidation of reaction products and achieve better product separation [8].

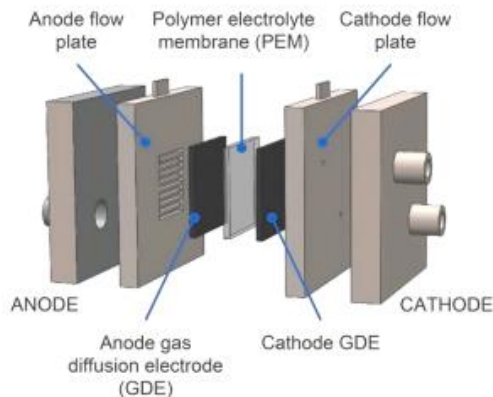


Figure 4. Membrane-based reactor with an MEA featuring anode and cathode gas diffusion electrodes [11].

2.3.1. Membrane electrode assembly

MEA is known as a composition of stacks of gas diffusion electrodes (GDE) and the catalyst at both the anode and cathode side with the membrane [12]. MEA is the weakest electrochemical component in a typical high-pressure PEM electrolyzer. The lower ionic resistance is received with the thinner membrane due to the higher voltage efficiency [13]. It is placed between the anodic and cathodic flow fields. The MEA is used as an ohmic overvoltage reduction of the cell by increasing the conductivity of the electrolyzer and the distance between the anode and cathode [8].

Vietnamese-German University

2.3.2. Gas diffusion electrodes

A typical gas diffusion layer (GDE) consists of a catalytic layer (CL), and a gas diffusion layer (GDL). CO_2 gas is transported from the gas diffusion layer to the catalytic layer through the porous tunnels by physical supports [14]. The GDE has lower mass transfer resistance and a larger active surface area than the planar electrode systems [8]. Lower current densities are achieved as the non-carbon formation of a GDE on the anode side in zero-gap reactors for CO_2 reduction [15].

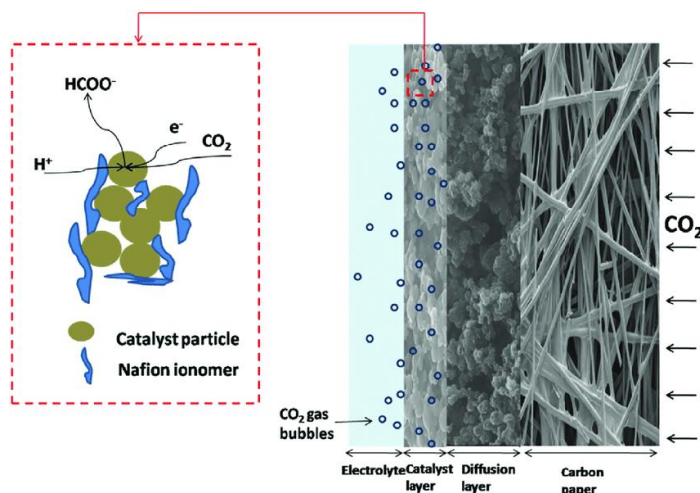


Figure 5. A simple structure of a gas diffusion electrode (GDE) [16].

Figure 5 illustrates the structure of a gas diffusion electrode. The GDL is hydrophobic and blocks the anolyte by its pores and facilitates the transportation to the CL [5]. The use of an electrocatalyst on the GDL creates a distant connection between the reactants and the catalyst surface [8], which create the reduction of the mass transfer of the CO₂, and maximizes the interaction among the reactant gas, catalyst, and solid ionomer [6].

2.3.3. Gas diffusion layer

The gas diffusion layer is the gas-permeable support structure where the CO₂ is guided to the catalyst layer. GDL controls the mass transfer of water, reactants, and products from and to the catalyst layer [17]. The gas diffusion layer consists of a macro-porous layer and, optionally, a microporous layer. The macro-porous layer allows the CO₂ to diffuse from the reactant to the catalyst surface. The membrane, which serves as the gas diffusion layer, involves an insulating microporous sheet with a hydrophobic PTFE fibers layer [17].

2.3.4. Catalyst layer

A catalyst is placed on the gas diffusion layer [17]. The catalyst layer is used to solve both kinetics and thermodynamics energy during the electrolysis process. With different current densities in the catalysts, the types of products are affected [6]. The local pH environment consequents the energetics of different CO₂ reduction reactor products. They provide secondary approaches to HER by weakening hydrogen energies [15]. Copper (Cu), gold (Au), zinc (Zn), palladium (Pd), gallium (Ga), nickel (Ni), and platinum (Pt) can be used as cathode catalysts [8]. On the anodic side, catalysts are made of iridium oxide or Pt, which helps the oxidation of water and improves the oxygen evolutionary reaction (OER) [6]. In addition, lead (Pb), mercury (Hg), indium (In), tin (Sn), cadmium (Cd), and thallium (Tl) are materials that are used as formic acid [8].

2.3.5. Membrane

The ion exchange membrane is used to separate the anode and cathode chambers. Three types of membranes are used in PEM electrolyzer: cation-exchange membrane (CEM), anion-exchange membrane (AEM), and bipolar membrane (BPM) [14]. The flow of the positive ions, which has the form of cation flow, is guided by a CEM from the anode to the cathode when the negative charges are held. Anions are transported from the cathode to the anode while the BPM splits the water combination to the anode and the cathode due to its structure [6].

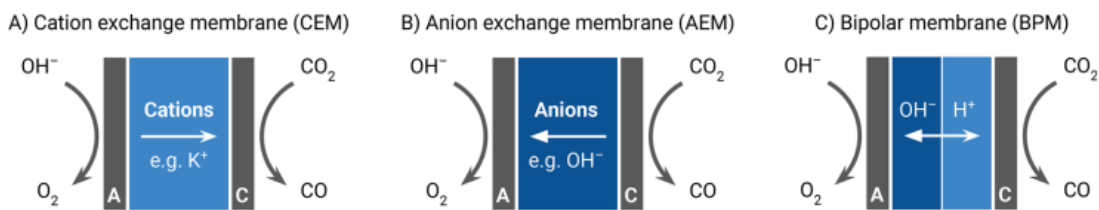


Figure 6. Types of different membranes [18].

2.4. Other components

In addition, the structure of the reactor includes anode and cathode flow fields, end plates, insulation layers, and current distributor.

Flow field

The flow field is used to aim a distribution of the reactants. The distribution is channeled to the gas diffusion layer (GDL) and subsequently directed to activate the catalyst layer within the MEA by the permeable electrode while maintaining a minimum pressure drop [19]. Circular and rectangular shapes are the most common cross-sections of the flow field. With the circular design, flow fields have more advantages when providing more homogeneous pressure on the active area [13]. The flow field is constructed with the fluid flow channels and bipolar plate on both the cathode and anode sides of the reactor.

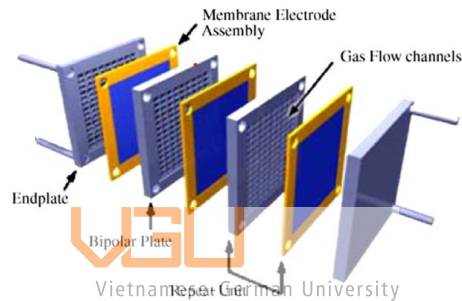


Figure 7. Stack components according to [2]

The fluid flow channels are used to guide the fluid flow. The size of flow field channels determines the distribution of CO_2 and H_2O delivered to the cathode and anode [15]. They are usually rectangular and have a width in the range of 1-2mm to minimize the fluid pressure loss due to friction losses [10]. **Figure 8** illustrates the types of flow channels. **Figure 8a** shows the serpentine flow channels. The fluid velocity in this type of channel is very high which can discharge the reaction products very fast. However, the resistance time is longer than other designs due to the long distance between the inlet and the outlet. The pressure drop in the serpentine flow channel design is also large which causes extra energy loss. **Figure 8b** presents the parallel design of the flow channels. The distance between the inlet and the outlet is shorter than the serpentine design so the pressure drop is reduced. However, there are some “dead zones” that appear in this design because of the block and accumulation of liquid. The interdigitated fluid flow channel design is shown in **figure 8c**. This design is more suitable for short-range circulation although the utilization rate of reactants and electrodes is lower [20].

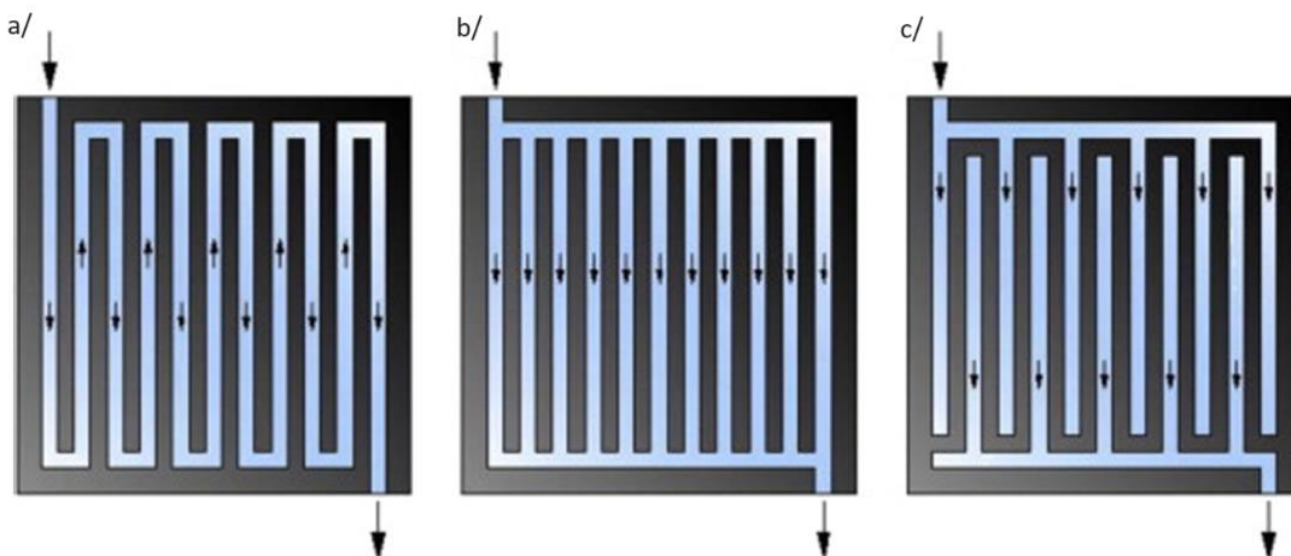


Figure 8. Common types of fluid flow channels a/ Serpentine fluid flow channels, b/ Parallel fluid flow channels, c/ Interdigitated fluid flow channels [20]

Bipolar plates are also called separator plates. They are one of the most important components to supply the reactant gases through the flow channels to the electrodes. These plates mechanically provide structure for weak MEAs and enhance water management within the electrochemical cell [10]. These plates work under harsh conditions. Bipolar plates also conduct the current and the conducting performance of the cell is determined by the electric contact resistance between the bipolar plates and the circuit distributor [21].

Circuit distributor

A circuit distributor is also called a copper plate. This plate serves not only as support elements but also for different purposes so it must be strong enough to work under high pressure. The circuit distributor must resist low electrical and contact. The anode copper plate works with high anodic potential so it must be corrosion resistance [13].

End plate

The end plate is used to hold either stacks or a CO₂ reduction reactor by compressing an appropriate pressure. In addition, the water and CO₂ inlets and outlets are connected to the end plate. The higher the pressure operated in the reaction, the thicker material is needed [13].

The CO₂ reduction reaction is very easily affected by small changes in the additional parameters of the atmosphere such as temperature, humidification, pressure, etc. Additionally, the different product selections were also collected from different process variables such as catalyst, pH, current densities, electrolyte type, flow properties, membrane, and concentration. The cell structure design also affects the value of products [8]. Water management is the main parameter that keeps the efficiency of CO₂ conversion constant [22].

3. State of the Art

3.1. CO₂ reduction in MEA-type Electrolyzers

A zero-gap electrolyzer is an electrolysis system that has no separation between cathodes, anodes, and electrolytes. The distance for the ion transportation is decreased due to the pressed and bonded layers. The zero-gap CO₂ electrolyzer delivered gaseous CO₂ to the cathode which helped them receive the high current densities [23]. In 2008, Delacourt developed a based CEM-CO₂ electrolyzer using a cathode catalyst made from silver, and this was the first CO₂ electrolysis carried out in this type of reactor. Unfortunately, the CO production was poor due to the acid environments, which was produced with the CEM [24]. **Figure 9** illustrates an overview construction of a zero-gap electrolyzer.

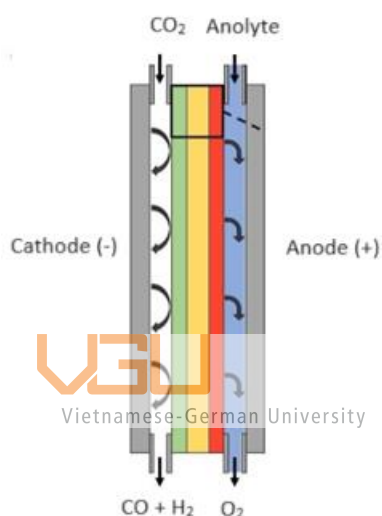


Figure 9. A zero-gap electrolyzer schematic according to [25].

3.2. Continuous PEM electrolyzer at Fraunhofer UMSICHT

At Fraunhofer UMSICHT, continuous CO₂ electrolysis is performed under 200 bar(g) pressure using a PEM electrolyzer in a zero-gap configuration. The reactor is used to carry out experiments with different current densities. According to **figure 10**, the construction of the existing reactor includes two end plates, two isolation layers, two copper conductivities, one cathode flow field, one anode flow field, two electrodes, and a membrane. Inlets and outlets for both CO₂ and water are attached to each end plate. The assembly involves the use of 10 M12 screws to fix the components together.

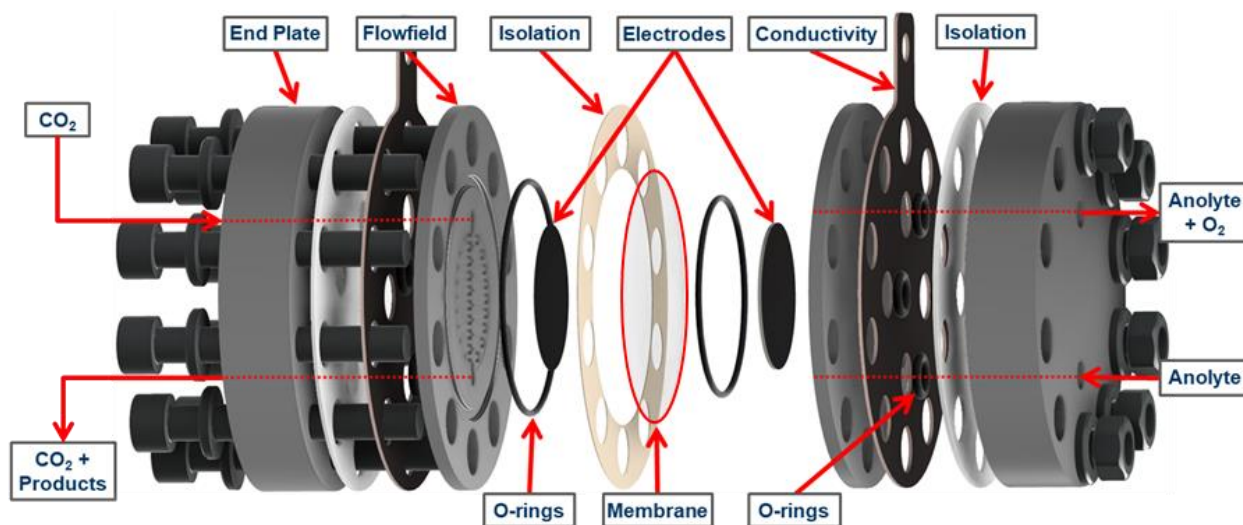


Figure 10. Configuration of the high-pressure electrolyzer at Fraunhofer UMSICHT.

The current reactor has an electrode diameter is 40 mm, which covers an electrode area of 12.57 cm². The mass flow of CO₂ in this reactor is in the range of 6 to 60 g h⁻¹ while the volume flow of H₂O is 80 ml min⁻¹. This zero-gap reactor is designed to operate under 200 bar(g) of pressure as well as ensure the safety and reliability in its construction. In addition, a circuit distributor is made of copper, enhancing the electrical conductivity. Insulating plates are used to insulate the electricity. **Table 1** below shows the technical information about the individual components.

Vietnamese-German University

Type	Material	Thickness	Function
End plate	Stainless steel	20mm	Mechanical stability
Flow field	Titanium	4mm	Fluid guidance
Circuit distributor	Copper	1mm	Current line
Insulating panel	Novapress®	1mm	Current insulating

Table 1. Overview information about the existing plates used in zero-gap reactors.

4. Objective

During the apply the use of the electrochemical CO₂ reactor in industry process, there are several decisive factors such as stability and cost efficiency of the electrolyzer as well as the scalability of the reactor architecture. However, the current zero-gap electrolyzer at Fraunhofer UMSICHT with its small reaction area of 12.57 cm² limits the CO₂ flow to 60 g h⁻¹.

In order to investigate the scalability zero-gap reactor design, the scale-up reactor aims to have the higher mass flow rate of the CO₂, which should be increased to about 1 kg h⁻¹ while the pressure condition is kept at 200 bar(g). The electrode area is increased 30 times bigger.

$$A_{new} = A_{existing} \cdot 30 = 12.57 \cdot 30 = 377.1 \approx 400 \text{ cm}^2$$

Equation 1. New electrode areas for scale-up reactor.

According to **equation 1**, the electrode working area is increased to 400 cm² in proportion to the CO₂ mass flow rate. However, with the 400 cm² working area of the electrodes, their diameter is 225.67 mm, which is too large to be constructed when it rejects the material-saving goals. The cell should be divided into small compartments in order to reduce the size of the reactor.

Diameter of electrodes (cm)	8	9	10	11	12
Area of electrodes (cm ²)	50.27	63.62	78.54	95.03	113.1
Number of stacks	8	7	6	5	4

Table 2. Selection of electrode diameter.

According to **table 2**, 8 compartments with a working area of 50 cm² for the electrodes, which leads to the diameter of each electrode now being 80mm. Each compartment includes an anode and a cathode flow field as well as a membrane electrode assembly (MEA), which consists of a membrane, and two electrodes with catalyst layers between the electrode and the membrane.

The way to center the components is also changed for the new design to reduce the cost of the stack construction. The components are centered by the M6 pins. In addition, the screws are used to center the end plates at both sides of the reactor. **Table 3** below shows the differences between the scale-up reactor and the existing one used at Fraunhofer UMSICHT.

	Existing reactor	Scale-up reactor
Working pressure	200 bar(g)	200 bar(g)
Mass flow of CO₂	6-60 g h ⁻¹	1 kg h ⁻¹
Volume flow of water (H₂O)	80 ml min ⁻¹	2500 ml min ⁻¹
Electrode diameter	40 mm	80 mm
Electrode area	12.57 cm ²	50 cm ²
Total electrode area	12.57 cm ²	400 cm ²
Number of compartments	1	8
Centering	M12 screws	Pins
Current density	300 mA cm ⁻²	300 mA cm ⁻²

Table 3. Comparison between the existing reactor and the aim for the scale-up one.

5. Stress calculation of the zero-gap reactor

For the design of the zero-gap reactor, several calculations are required to ensure an operating pressure of 200 bar(g). First, the tightness of the sealing is calculated in **section 5.1** according to AD 2000 [26]. Then, **section 5.2** describes the calculation for the thickness of the end plates regarding to DIN EN 13445-3 [27]. **Section 5.3** shows the radial wall thickness of the components such as flow fields, copper plate according to DIN EN 13445-11 [28] and 13445-12 [29]. The screw selection is determined in **section 5.4** by the technical numbers and strength calculations according to Roloff/Matek [30]. **Section 5.5** illustrates the pins technical specifications and calculations, which are taken from JIS B0401-2 [31].

5.1. Tightness of the sealing according to AD2000

In this section, the tightness of the sealing and the number of screws, that are constructed in the end plate are determined according to AD2000. In addition, the technical number of the O-ring and the washers are taken from DIN ISO 3601-2 and GN 6339.

The core diameter of the screws that are constructed in the end plate $d_{k_{BZ}}$ is calculated with the determination of the auxiliary quality z_{BZ} , the bolt force for the operating condition F_{SB} , number of screws n_{screws} , yield strength of the screw class $k_{12,9}$ and the design allowance c_5 .

$$d_{k_{BZ}} = z_{BZ} \cdot \sqrt{\frac{F_{SB}}{k_{12,9} \cdot n_{screws}}} + c_5$$

Equation 2. The thread core diameter construction of the end plate.

The design allowance c_5 depends on the minimum bolt force for the operating condition F_{SB} based on the leaflet AD2000 B7 [26]. If the condition from **equation 3** is smaller than 20mm, the design allowance is $c_5 = 3 \text{ mm}$, whether the design allowance is $c_5 = 1 \text{ mm}$.

$$z_{BZ} \cdot \sqrt{\frac{F_{SB}}{k_{12,9} \cdot n_{screws}}}$$

Equation 3. Condition for design allowance determination [26].

The auxiliary quality is defined by the determination of the safety operation condition S_0 , the auxiliary value for parallel bearings μ_{EP} .

$$z_{BZ} = \sqrt{\frac{4 \cdot S_0}{\pi \cdot \mu_{EP}}}$$

Equation 4. Auxiliary quality

The bolt force for operating condition F_{SB} is calculated based on the minimum bolt force elements F_{RB}, F_{FB}, F_{DB} of the equations in leaflet AD2000 B7 [26].

$$F_{SB} = F_{RB} + F_{FB} + F_{DB}$$

Equation 5. The bolt force for operating conditions based on [26].

$$F_{RB} = p \cdot \frac{\pi}{4} \cdot d_i^2$$

Equation 6. Minimum bolt force element based on [26].

$$F_{FB} = p \cdot \frac{\pi}{4} \cdot (d_D^2 - d_i^2)$$

Equation 7. Minimum bolt force element based on [26].

$$F_{DB} = p \cdot \pi \cdot d_{FL} \cdot S_D \cdot k_{1FL}$$

Equation 8. Operating sealing force based on [26].

From **equations 5, 6, 7, and 8**, the shortened equation is:

$$F_{SB} = p_{zul} \cdot \left(\frac{\pi}{4} \cdot d_{DFL}^2 + \pi \cdot d_{DFL} \cdot S_D \cdot k_{1FL} \right) = p_{zul} \cdot \frac{y_1}{y_2} \cdot \frac{\pi}{4} \cdot G_0^2$$

Equation 9. The bolt force for operating condition.

Due to the use of an O-ring, the characteristic value $k_{1FL} = 0$ in the operating condition, and the bolt force is increased due to the lever arm ratio y_1/y_2 , the bolt force for the operating condition is:

$$F_{SB} = p_{zul} \cdot \frac{y_1}{y_2} \cdot \frac{\pi}{4} \cdot G_0^2$$

Equation 10. Shortened bolt force for operation condition.

According to **Figure 1 of the appendix**, the mean seal diameter G_0 is the sum of the inner diameter of the larger O-ring d_1 and the core size d_2 . The mean seal diameter G_0 is:

$$G_0 = d_1 + d_2 = 101.32 + 1.78 = 103.1 \text{ mm}$$

Equation 11. Mean seal diameter.

The lever arm $y_1 = 89 \text{ mm}$ when it is measured from the outer edge of the end plate to the center of the wall thicknesses of the container, while the lever arm $y_2 = 15 \text{ mm}$ when it is measured from the outer edge to the bolt pitch diameter [26]. **Figure 11** illustrates the measuring guide.

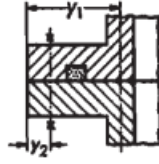


Figure 11. The O-ring gasket characteristic [26].

The ratio between the two lever arms is:

$$\frac{y_1}{y_2} = \frac{66.5}{15} = 4.43$$

Equation 12. Lever arm ratio.

The operating pressure $p_{zul} = 200 \text{ bar}(g) = 20 \text{ MPa}$ and the mean seal diameter $G_0 = 103.1 \text{ mm}$. The bolt force for the operating condition is:

$$F_{SB} = 20 \cdot 4.43 \cdot \frac{\pi}{4} \cdot 103.1^2 = 740231.55 \text{ N}$$

Equation 13. The bolt force for operating condition.

According to table 1 of GN 6339, the diameter of the washers for M16 screws is determined from **table 1 of the appendix** with $d_{washers} = 30 \text{ mm}$ [32].

The minimum number of screws that can be assembled to the cell is calculated:

$$n_{screws} \geq \frac{\pi \cdot C_{HD}}{5 \cdot d_B} = \frac{\pi \cdot 205}{5 \cdot 16} = 8.05 \approx 9 \text{ screws}$$

Equation 14. Minimum number of screws [26,33].

The reactor should be designed to assemble easily and quickly in order to save time during the experiments. To accomplish that, the number of screws is assumed $n_{screws} = 16 \text{ screws}$.

The zero-gap reactor has two end plates at both sides of the cell to hold and center the compartments. The end plate calculation includes the calculations of the diameter and the core thread diameter of the end plate.

The minimum diameter of the end plate is the sum of the pitch diameter of the screws and the diameter of the washers.

$$d_{endplate} = C_{HD} + d_{washer} = 205 + 30 = 235 \text{ mm}$$

Equation 15. Minimum diameter of the end plate.

The safety factor of the operation condition is $S_0 = 1.8$. According to AD2000 B7, the auxiliary value for parallel bearings of the end plate is $\mu_{EP} = 1$. The auxiliary quality is calculated:

$$z_{BZ} = \sqrt{\frac{4 \cdot S_0}{\pi \cdot \mu_{EP}}} = \sqrt{\frac{4 \cdot 1.8}{\pi \cdot 1}} = 1.51$$

Equation 16. Auxiliary quality [26].

$$z_{BZ} \cdot \sqrt{\frac{F_{SB}}{k_{12.9} \cdot n_{screws}}} = 1.51 \cdot \sqrt{\frac{740231.55}{1080 \cdot 16}} = 9.88 \text{ mm} \leq 20 \text{ mm}$$

Equation 17. Condition for design allowance determination.

From **equation 17**, the condition is smaller than 20mm, and the design allowance $c_5 = 3\text{mm}$. The thread core diameter of the end plate is:

$$d_{k_{BZ}} = z_{BZ} \cdot \sqrt{\frac{F_{SB}}{k_{12.9} \cdot n_{screws}}} + c_5 = 1.51 \cdot \sqrt{\frac{740231.55}{1080 \cdot 16}} + 3 = 12.88 \text{ mm}$$

Equation 18. The thread core diameter construction of the end plate.

Compared to the thread core diameter $d_{k_{BZ}}$ of the core diameter of the M16 screw d_3 , $d_{k_{BZ}} = 12.88 \text{ mm} \leq d_3 = 13.546 \text{ mm}$, it is acceptable with 16 M16 screws and can be constructed.

5.2. Calculation of axial wall thickness of the end plate

In this section, the minimum thickness of the end plates is calculated. In addition, the calculations are related to the tightness of the reactor according to AD 2000 B7, and B8. At least four screws have to be used and the screw pitch distance should not be larger than $5 \cdot d_B$ [26]. The minimum thickness e_A for the installed condition is determined in section 10.5.2 of DIN EN 13445-3 [27]. This equation includes the determination of the pitch circle diameter of screws C_{HD} , the mean diameter of the seal G_0 , the designed bolt load w_A , and the internal stress of the material f_A .

$$e_A \geq \sqrt{\frac{3 \cdot (C_{HD} - G_0) \cdot w_A}{\pi \cdot G_0 \cdot f_A}}$$

Equation 19. The minimum thickness of the end plate for the installed condition [27].

The installation width of the sealing b_4 and the characteristic value y_0 are used to calculate the designed bolt load for installed condition w_A . The designed bolt load for the installed condition equation w_A is.

$$w_A = \pi \cdot b_4 \cdot G_0 \cdot y_0$$

Equation 20. The bolt load for the installed condition [27].

Tensile strength and 1%-yield strength at room temperature can be found in Table 8 of DIN EN 10088-3. The tensile strength is $R_{m/T} = R_{m/RT} = 500 \text{ MPa}$, and the 1%-yield strength is

$R_{p\ 1,0/T} = R_{p\ 1,0/RT} = 235\ MPa$ [34]. The calculation of the internal stress of material at the room temperature f_A is:

$$f_A = \max \left[\left(\frac{R_{p1,0/T}}{1.5} \right); \min \left(\frac{R_{p1,0/T}}{1.2}; \frac{R_{m/T}}{3} \right) \right]$$

Equation 21. Internal stress of the material.

$$f_A = \max \left[\left(\frac{235\ MPa}{1.5} \right); \min \left(\frac{235\ MPa}{1.2}; \frac{500\ MPa}{3} \right) \right] \approx 166.67\ MPa$$

Equation 22. The internal stress of the material.

The mean pitch t_B can be determined by the screw pitch diameter C_{HD} and the number of screws n_{screws} .

$$t_B = \frac{\pi \cdot C_{HD}}{n_{screws}}$$

Equation 23. The mean pitch of screws.

The M16 bolts are used to center the end plates at both sides of the new reactor. This selection can save the material and be cost-effective. The screw diameter of the M16 screws is $d_B = 16\ mm$.

The screw pitch diameter is $C_{HD} = 205\ mm$, and the number of screws is assumed $n_{screws} = 16\ screws$. The mean pitch of screws is now determined:

$$t_B = \frac{\pi \cdot C_{HD}}{n_{screws}} = \frac{\pi \cdot 205}{16} = 40.25\ mm$$

Equation 24. The mean pitch of screws.

The minimum thickness of the end plate is also found in section 10.5.2 of DIN EN 13445-3 [27].

$$e_{cell} = \max(e_A; e_{p_1})$$

Equation 25. The minimum thickness of the end plate.

The minimum wall thickness of the end plates with the operation condition e_{p_1} is known with the values of the correction factor $C_{F_{cell}}$, the mean diameter of the sealing G_0 , the operating pressure p_{zul} , the internal stress of the material, the width and the factor of the flat gasket b_{Fl} , m_{Fl} . The minimum wall thickness of the end plates for the operation condition is:

$$e_{p_1} \geq \sqrt{\left[3 \cdot C_{F_{cell}} \left(\frac{G_0}{4} + 2 \cdot b_{Fl} \cdot m_{Fl} \right) (C_{HD} - G_0) \right] \frac{p_{zul}}{f}}$$

Equation 26. The minimum thickness of the end plate with operation condition [27].

The designed bolt load for the assembled condition equation is:

$$w_A = \pi \cdot b_4 \cdot G_0 \cdot y_0 = \pi \cdot 2.9 \cdot 103.1 \cdot 2.52 = 2367.05 \text{ N}$$

Equation 27. Designed bolt load for the assembled condition [27].

According to **equation 25**, the e_{cell} is determined based on e_A and e_{p_1} . However, the e_{p_1} is calculated based on the $C_{F_{cell}}$. The second term of the correction factor is applied with $C_{F_{cell}} = 1$ when the wall thickness of the end plates $e_{cell} < 6 \text{ mm}$. Now, the minimum thickness of the end plates for the installation condition is calculated.

$$e_A \geq \sqrt{\frac{3 \cdot (C_{HD} - G_0) \cdot w_A}{\pi \cdot G_0} \cdot \frac{1}{f_A}} = \sqrt{\frac{3 \cdot (205 - 103.1) \cdot 2367.05}{\pi \cdot 103.1} \cdot \frac{1}{166.67}} = 3.66 \text{ mm} \approx 3.7 \text{ mm}$$

Equation 28. The minimum thickness for the installed condition [27].

The required wall thickness of the end plates for the operating condition is:

$$e_{p_1} \geq \sqrt{\left[\frac{3 \cdot (3 + \nu)}{32} G_0^2 + 3 \cdot C_{F_{cell}} \left(\frac{G_0}{4} + 2 \cdot b_{Fl} \cdot m_{Fl} \right) (C_{HD} - G_0) \right] \frac{p_{zul}}{f_A}}$$

Equation 29. The minimum thickness of the end plate with operation condition [27].

During the operation, the maximum temperature is $T_{max} = 100^\circ \text{C}$. The temperature-dependent 1% proof stress at room temperature can be found in Table 20 of DIN EN 10088-3. The tensile strength is $R_{m/T} = R_{m/RT} = 200 \text{ MPa}$ and the 1% yield strength is $R_{p\ 1,0/T} = R_{p\ 1,0/RT} = 430 \text{ MPa}$ [34]. The calculation of internal stress of material at the room temperature f_A .

$$f_A = \max \left[\left(\frac{200 \text{ MPa}}{1.5} \right); \min \left(\frac{200 \text{ MPa}}{1.2}; \frac{430 \text{ MPa}}{3} \right) \right] \approx 144.33 \text{ MPa}$$

Equation 30. The internal stress of the material at room temperature.

According to table 12.6b of Roloff-Matek, the Poisson ratio for steel is $\nu = 0.3$ [30]. The operating pressure is $p_{zul} = 200 \text{ bar} = 20 \text{ MPa}$. In addition, the flat gasket of the existing reactor is replaced by the O-ring for the new design, so $b_{Fl} = 0$. The minimum wall thickness for the operating condition is:

$$e_{p_1} \geq \sqrt{\left[\frac{3 \cdot (3 + 0.3)}{32} \cdot 103.1^2 + 3 \cdot 1 \left(\frac{103.1}{4} \right) (205 - 103.1) \right] \frac{20}{144.33}} = 39.33 \text{ mm} \approx 39.4 \text{ mm}$$

Equation 31. The minimum thickness of the end plate with operation condition.

According to **equations 25,28 and 31**, the minimum wall thickness for the end plates is:

$$e_{cell} = \max(e_A; e_{p_1}) = \max(3.38; 39.4) = 39.4 \text{ mm}$$

Equation 32. The minimum thickness of the end plate.

Overall, the minimum wall thickness of the end plate is $e_{cell} = 39.4 \text{ mm}$. However, the wall thickness of the end plate is rounded up to $e_{cell} = 40 \text{ mm}$ in order to manufacture easily.

5.3. Calculation of the radial wall thickness of the components

In this section, the radial wall thickness of the components such as flow fields and copper plates are calculated in order to determine the size of the reactor's components. The outer diameter of the flow fields as well as the copper plate $D_{a_{components}}$ is known as the sum of the inner diameter of the component and the radial wall thickness $e_{components}$. The inner diameter of the component $D_{i_{components}}$ is measured from the center of the component to the outer diameter of the inlet and outlet.

$$D_{a_{components}} = D_{i_{components}} + 2 \cdot e_{components}$$

Equation 33. The outer diameter of the components.

$$e_{components} = \max(e_{flow \text{ fields}}; e_{copper \text{ plates}})$$

Equation 34. The radial wall thickness of the components.

$$e = \frac{p_{zul} \cdot D_{i_{components}}}{2 \cdot f_A \cdot z - p_{zul}}$$

Equation 35. The radial wall thickness based on [27].

According to table 1 of DIN EN 17861, the 1% yield strength at the room temperature of the titanium material Ti2 is $R_{p1,0/T} = 270 \text{ MPa}$, and the tensile strength is $R_{m,T} = 540 \text{ MPa}$ [35]. The inner diameter of the components is measured from the center of the flow field to the outer diameter of the inlets and outlets $D_{i_{components}} = 147 \text{ mm}$. The internal stress of the titanium material is calculated based on table 6.4.1 of DIN EN 13445-11 [28]:

$$f_A = \min\left(\frac{R_{p1,0/T}}{1.5}; \frac{R_{m/T}}{3}\right) = \min\left(\frac{270}{1.5}; \frac{540}{3}\right) = 180 \text{ MPa}.$$

Equation 36. The internal stress of the titanium material.

The radial wall thickness of the flow field is:

$$e_{flow \text{ field}} = \frac{p \cdot D_{i_{components}}}{2 \cdot f_A \cdot z - p} = \frac{20 \cdot 147}{2 \cdot 180 - 20} = 8.65 \text{ mm} \approx 8.7 \text{ mm}$$

Equation 37. The radial wall thickness of the flow field.

The tensile strength of the copper material is found in table 9 of DIN EN 12449 with $R_{m/T} = 360 \text{ MPa}$ [36]. The internal stress of the copper material is calculated based on table 6.2.1-2 of the DIN EN 13445-12 [29]:

$$f_A = \frac{R_{m/T}}{3} = \frac{360}{3} = 120 \text{ MPa}$$

Equation 38. The internal stress of the copper material.

The radial wall thickness of the copper plate is:

$$e_{copper\ plate} = \frac{p \cdot D_{i\ components}}{2 \cdot f_A \cdot z - p} = \frac{20 \cdot 147}{2 \cdot 120 - 20} = 13.36 \text{ mm} \approx 13.4 \text{ mm}$$

Equation 39. The radial wall thickness of the copper plate.

According to **equation 34**, the radial wall thickness of the components is:

$$e_{components} = \max(e_{flow\ field}, e_{copper\ plate}) = \max(8.7; 13.4) = 13.4 \text{ mm}$$

Equation 40. The radial wall thickness of the components.

The minimum diameter of the components is:

$$D_{a\ components} = D_{i\ components} + 2 \cdot e_{components} = 147 + 2 \cdot 13.4 = 173.8 \text{ mm}$$

Equation 41. The outer diameter of the components.

In conclusion, the minimum diameter of the components such as copper plate, flow field is $D_{a\ components} = 173.8 \text{ mm}$. However, this diameter is rounded up to $D_{a\ components} = 175 \text{ mm}$ in order to ensure the stability during the operation.

Vietnamese-German University

5.4. Screw strength calculation according to Roloff/Matek

The cylindrical socket head screws M16, class 12.9 are used to maximize the operating pressure of the cell. This section will illustrate the calculations of the cell's components. The required stress cross-section of the screws A_s must be calculated according to the operating pressure.

$$A_s \geq \frac{F_B + F_{KL}}{\frac{k_{12.9}}{\kappa \cdot k_A} - \beta \cdot E \cdot \frac{f_z}{l_k}}$$

Equation 42. The require stress cross section.

The permissible operating force F_B is calculated from the formula of the operating pressure p_{zul} with the loaded cross-section A_{last} and the number of screws n_{screws} .

$$F_B = \frac{p_{zul} \cdot A_{Last}}{n_{screw}}$$

Equation 43. The operating force for the screws.

The operating pressure of the cell is $p_{zull} = 200 \text{ bar}$, number screws n_{screws} , the clamping length of the cell l_k , the set amount of the cell, and the yield strength of screws class $k_{12.9}$, which is determined in **table 2 of the appendix**.

According to the Roloff-Matek, the technical numbers of M12 and M16 screws are known [30]. The core diameter d_3 and the load cross-section A_s are taken from Roloff-Matek TB 8-1, while the head surface area A_p is taken from Roloff-Matek TB 8-9. The total friction coefficient μ_g (static friction) and μ_k (kinetic friction) are taken from Roloff-Matek TB 8-12. The tightening force F_{sp} and the tightening torque M_{sp} are taken from Roloff-Matek TB 8-14.

The yield strength of the class 12.9 screws is $K_{M16} = 1080 \text{ MPa}$ according to TB 8-4 of Roloff-Matek [30]. The pressure surface of the M16 cylindrical socket head screw is calculated:

$$P_{FP \text{ M16}} = \frac{F_{SP \text{ M16}}}{0.9 \cdot A_{P \text{ M16}}} = \frac{135 \cdot 1000}{0.9 \cdot 181} = 828.73 \text{ MPa}$$

Equation 44. The pressure surface of the screws [30].

The loaded diameter d_{last} is measured as the diameter from the outer edge of the support channels, with $d_{last} = 153.75 \text{ mm}$. The clamping length l_k is the sum of the wall thickness of the components.

$$l_k = 40 \cdot 2 + 2 \cdot 2 + 1 \cdot 2 + (8 + 8) \cdot 8 = 214 \text{ mm}.$$

Equation 45. Clamping length.

The roughness of the components of the cell is assumed, $40 \leq R_z < 160 \mu\text{m}$. The set amount f_z is the sum of the set amount of thread, the set amount of head or nut support, and the set amount of inner parting line.

$$f_z = f_{z_{thread}} + f_{z_{head \text{ or } nut \text{ support}}} + f_{z_{inner \text{ parting line}}}$$

Equation 46. The total set amount [30].

According to TB 8-10 of Roloff-Matek, the roughness quality from 40 to 60 μm provides the set amount for thread is $f_{z_{thread}} = 3 \mu\text{m}$, the set amount for one head or nut support is $f_{z_{head \text{ or } nut}} = 4 \mu\text{m}$, and the set amount for one inner parting line is $f_{z_{parting \text{ line}}} = 3 \mu\text{m}$. The cell consists of 8 compartments, 2 copper plates, 2 insulations, and 2 end plates, which are tightened by screws. Each compartment has 2 flow fields, 1 gas diffusion layer, and 1 membrane. The set amount of the cell is:

$$f_{z_{head \text{ or } nut \text{ support}}} = 2 \cdot f_{z_{per \text{ head \text{ or } nut \text{ support}}}}$$

Equation 47. The set amount of head or nut support.

$$f_{z_{inner \text{ parting line}}} = (n_{components} - 1) \cdot f_{z_{per \text{ inner parting line}}}$$

Equation 48. The set amount of the inner parting line.

$$f_z = 3 + 4 \cdot 2 + 3 \cdot ((2 + 1 + 1) \cdot 8 + 2 + 2 + 2 - 1) = 122 \mu\text{m} = 0.122 \text{ mm}$$

Equation 49. The total set amount.

The loaded cross-section area of the cell is

$$A_{last} = \frac{\pi \cdot D_{last}^2}{4} = \frac{\pi \cdot 153.75^2}{4} = 18566 \text{ mm}^2$$

Equation 50. The loaded cross-section area.

The operating force for the screws is calculated:

$$F_B = \frac{p_{zul} \cdot A_{Last}}{n_{screw}} = \frac{20 \cdot 18566}{16} = 23207.5 \text{ N}$$

Equation 51. The operating force for the screws.

According to Roloff-Matek Formelsammlung, the reduction factor $\kappa = 1.24$ and compliance factor $\beta = 0.8$ for $\mu_G = 0.14$ [37]. The dressing factor k_A is taken from TB 8-11 of Roloff-Matek with $k_A = 1.6 \dots 2.5$ and $k_A = 2.5$ is taken. The Young modulus of steel, the material of the screws, $E = 210000 \text{ MPa}$ [30]. The clamping force is assumed to be $F_{KL} = 0$.

$$A_s \geq \frac{F_B + F_{KL}}{\frac{k_{12.9}}{\kappa \cdot k_A} - \beta \cdot E \cdot \frac{f_z}{l_k}} = \frac{23207.5}{\frac{1080}{1.24 \cdot 2.5} - 0.8 \cdot 210000 \cdot \frac{0.122}{214}} = 91.87 \text{ mm}^2$$

Equation 52. The operating pressure.

Compared to the actual stress cross section for the M16 screws, $A_{SM16} = 157 > 91.87 \text{ mm}^2$, which means the size and the number of screws is acceptable for the cell design.

5.5. Calculation of pins

M6 pins are used to center the compartments of the cell. According to table 1 of JIS B0401-2, the types of fitting pins are determined. The pins used in the cell are to center the compartments of the cell as well and they need to be removed easily, which means, the pins are type H7-f7 in table 1 of JIS B0401-2. The pins diameter is 6 mm, the tolerance of the shaft is from -10 to -22 μm and the tolerance of the hole is +12 μm [31].

6. Calculation of fluid channels

In this chapter, the parameters of the fluid channels are determined in order to maintain the laminar flow type of the fluid as well as select the size of the O-rings.

O-rings are used to seal the interfaces and prevent the leakage of gas or liquid in the CO₂ reduction reaction process. They are also used to maintain the efficiency and performance of the zero-gap electrolyzer. According to DIN ISO 3601-2, table 6, the width of the O-ring installation space $b_4 = 2.9 \text{ mm}$ for the gas phase and $b_4 = 3.2 \text{ mm}$ for the liquid phase [38]. In addition, the depth of the O-ring installation space is also determined. **Figure 2 of the appendix** illustrates the cross-section parameters of the sealing covered by walls on both sides. **Figure 3 of the appendix** shows the cross-section parameters of the sealing without covering. An outer diameter of the installation space with sealing d_7 and an inner diameter of the installation space with sealing d_8 are also shown in 2 figures. The size and parameters of the O-ring are determined by Table 7 in DIN ISO 3601-2. The O-ring selections for the anode and cathode flow fields are based on the parameters of CO₂ and water inlet, outlet, and the diameter of electrodes. The diameter of the CO₂ and water inlet, outlet is calculated for the laminar flow condition in the cell. The properties of CO₂ and water are found on the NIST and Fluidat website. In this chapter, the calculations for O-ring selections are shown.

6.1. O-ring selections for electrode flow field

According to **table 2 of chapter 3**, the selected diameter for the electrodes is 80 mm, and the scale-up reactor will have 8 stacks. The wall thickness between the electrodes and the O-ring is 9.5 mm at the anode and 3.2 mm at the cathode flow field. The inner diameter for the anode flow field O-ring is $d_1 = 101.3 \text{ mm}$, and the inner diameter for the cathode flow field O-ring is $d_1 = 88.62 \text{ mm}$. The core size for both O-rings is $d_2 = 1.78 \text{ mm}$.

6.2. Scaling parameter of CO₂ stream

The diameter of the CO₂ inlet and outlet is determined by the flow condition. The CO₂ flows into the reactor is typically laminar flow under the flow condition. The type of flow is determined in this section as well as the diameter of the gas inlet, outlet. The density and dynamic viscosity parameters of CO₂ are determined from the NIST and Fluidat website [39,40].

In order to classify the type of flow condition, the Reynolds number must be determined using parameters such as density, dynamic viscosity, velocity, and the area of the gas inlet or outlet. If the Reynolds number is lower than 2300, the flow condition is laminar. The flow condition is mix-type when the Reynolds number is between 2300 and 10^5 . The turbulent flow exists when the Reynolds number is larger than 10^5 [41].

$$Re = \frac{\rho \cdot v \cdot d_{inlet/outlet}}{\mu}$$

Equation 53. Reynolds number [41].

The mass flow of the inlet and outlet is proportional to the electrode area. The mass flow for CO₂ at the inlet and inlet will be increased to:

$$\dot{m}_{scale-up} = \frac{A_{new}}{A_{exist}} \cdot \dot{m}_{exist} = \frac{400}{12.57} \cdot 36 = 1145 \text{ g h}^{-1} \approx 1.2 \text{ kg h}^{-1}.$$

Equation 54. Mass flow for the scale-up reactor.

The velocity of the CO₂ flow is:

$$v = \frac{\dot{m}_{scale-up}}{\rho \cdot A_{inlet/outlet}}$$

Equation 55. Velocity of the flow [41].

Assumed the diameter of the inlet and outlet diameter of the CO₂ in the cell is $d_{inlet/outlet} = 12 \text{ mm}$. The area of the inlet and outlet of CO₂ in the cell will be:

$$A_{inlet/outlet} = \pi \cdot \frac{d_{inlet/outlet}^2}{4} = \pi \cdot \frac{12^2}{4} = 113.1 \text{ mm}^2 = 0.000113 \text{ m}^2$$

Equation 56. Area of the inlet and outlet of CO₂ flow.

According to the density determined in **table 4 of the appendix, equation 53, and equation 55**, the velocity and the flow type of the CO₂ at the inlet and outlet of the flow fields are determined.

The Reynolds numbers in **table 7 of the appendix** are determined based on **equation 53, table 4, table 5, table 6 of appendix**, and the assumed diameter of the inlet and outlet for CO₂ flow in the flow fields. According to **table 7 of the appendix**, the $d_{inlet/outlet} = 12 \text{ mm}$ is unsuitable due to the mix flow condition occurring at 25⁰C under 0 to 20 bar (g) condition. The assumed inlet and outlet diameter for CO₂ flow is increased to $d_{inlet/outlet} = 13 \text{ mm}$. The area of the inlet and outlet will be $A_{inlet/outlet} = 132.72 \text{ mm}^2$.

According to **table 8 of the appendix**, the flow type is a laminar flow for all conditions of pressure as well as temperature. The minimum diameter for the inlet and outlet of CO₂ flow is $d_{inlet/outlet} = 13 \text{ mm}$. The structure for the O-ring holder for the CO₂ flow inlet and outlet is an individual wall for the outer diameter of the installation space d_7 . The 15.6x1.78 size of the O-ring is selected based on DIN ISO 3601-2 [38].

6.3. Scaling parameter of water stream

The diameter of the water inlet and outlet is also determined by the flow type of the water. The properties of water and the calculations, which can define the water flow type, are shown in this section. The water properties data is collected from the NIST website [40].

The volume flow of water at the inlet and outlet is proportional to the electrode area. The volume flow at the inlet and outlet of the existing reactor is 80 ml min^{-1} . The volume flow of water in the scale-up reactor will be:

$$\dot{V}_{scale-up} = \frac{A_{new}}{A_{exist}} \cdot \dot{V}_{exist} = \frac{400}{12.57} \cdot 80 = 2545 \text{ ml min}^{-1} \approx 2.5 \text{ l min}^{-1}$$


Equation 57. Volume flow of water for scale-up reactor.

The volume flow for each compartment will be:

$$\dot{V}_{scale-up} = \frac{\dot{V}_{scale-up}}{n_{compartments}} = \frac{2.5}{8} = 0.3125 \text{ l min}^{-1} = 5.2 \cdot 10^{-3} \text{ l s}^{-1}$$

Equation 58. Volume flow of water per compartment.

Assumed the diameter of the inlet and outlet for the water flow is $d_{water} = 6 \text{ mm}$, the area of the inlet and outlet is:



$$A_{water} = \pi \cdot \frac{d_{water}^2}{4} = \pi \cdot \frac{6^2}{4} = 28.27 \text{ mm}^2 = 28.27 \cdot 10^{-4} \text{ dm}^2$$

Equation 59. The water inlet and outlet area.

The velocity of the water flow is:

$$v_{water} = \frac{\dot{m}_{scale-up}}{\rho \cdot A_{water}} = \frac{\dot{V}_{scale-up}}{A_{water}} = \frac{5.2 \cdot 10^{-3}}{28.27 \cdot 10^{-4}} = 1.84 \text{ dm s}^{-1} = 184 \text{ mm s}^{-1}$$

Equation 60. Velocity of water flow.

The Reynolds number is calculated based on **equation 53**, and the type of flow condition is determined.

According to **table 9, and table 10 of the appendix**, the Reynolds numbers and the type of water flow are determined in **table 11 of the appendix**. The results shown in **table 11 of the appendix** verify that the diameter of the inlet and outlet for water flow $d_{water} = 6 \text{ mm}$ is unsuitable due to the mix flow condition at 60°C . The assumed water flow inlet and outlet diameter is increased to $d_{water} = 7 \text{ mm}$. The area of the water inlet and outlet will be $A_{water} = 38.48 \text{ mm}^2 = 38.38 \cdot 10^{-4} \text{ dm}^2$. The velocity of the water flow is $v_{water} = 135.34 \text{ mm s}^{-1}$.

According to **table 12 of the appendix**, the flow type is the laminar flow for all conditions of pressure as well as temperature. The minimum diameter for the inlet and outlet of water flow is $d_{water} = 7 \text{ mm}$. However, the decision to acquire the same size of O-ring for both CO₂ and water inlets and outlets, the diameter of inlets and outlets is increased to $d_{water} = 13 \text{ mm}$. The Reynolds number and the classification of flow condition are carried out with the new diameter. The area of the water flow inlet and outlet will be $A_{water} = 132.73 \text{ mm}^2$ and the velocity of water flow is $v_{water} = 39.24 \text{ mm s}^{-1}$.

The flow types of water, which are shown in **table 13 of the appendix** verify that the diameter of the water flow inlet and outlet $d_{water} = 13 \text{ mm}$ is acceptable. The structure for the O-ring holder for the water flow inlet and outlet is an individual wall for the outer diameter of the installation space d_7 . The 15.6x1.78 size of the O-ring is selected for both CO₂ and water flow inlet and outlet based on DIN ISO 3601-2 [38].

The distance between the CO₂ inlet and outlet and the water inlet and outlet is 33.55 mm. The 41x1.78 size of the O-ring is selected for this installation room. The inner diameter of this size of O-ring is $d_1 = 41 \text{ mm}$, and the outer wall of the installation space is $d_7 = 44.55 \text{ mm}$ [38].

7. Additional parameters

Most of the main calculations for the design are shown in **Chapter 5**. Nevertheless, to certain the validity and the practicality of the design, there are extended parameters such as screws, nuts, and manufacturing methods that must be determined.

7.1. Screws and nuts

In order to tighten the screws, nuts are attached to the end plate on the other side of the cell. According to DIN 934, the technical data for the nuts are determined [42].

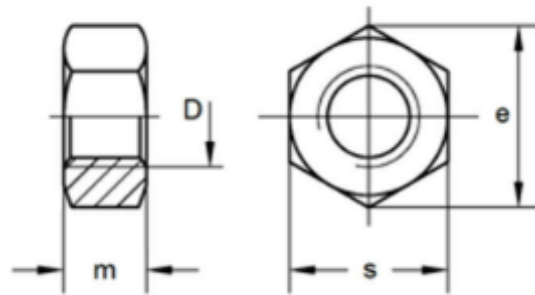


Figure 12. Cross-section of the nut design [42].



Figure 13. CAD M16 hex nut.

According to **table 14 of the appendix**, the thickness for the M16 hexagon nut is $m_{nut} = 13 \text{ mm}$, the width of the nut is $s_{nut} = 24 \text{ mm}$, and the height of the nut is $e_{nut} = 26.8 \text{ mm}$. The size of a hexagon socket is also determined to measure the distance between screws. The mean pitch of the screws must be larger than the diameter of the hexagon socket indoors to fit the socket. Misumi provides the technical data for the hexagon socket [43].

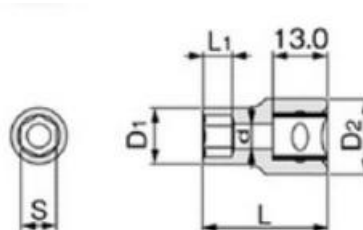


Figure 14. Cross-section of the hexagon socket design [43].

According to **table 15 of the appendix**, the outer diameter of the hexagon socket is $D_2 = 32 \text{ mm}$ is suitable for the M16 hexagon nut when its width is $s_{nut} = 24 \text{ mm}$. The diameter of the connection tools to the hexagon socket is $D_1 = 25.5 \text{ mm}$, the total length of the hexagon socket is $L = 34 \text{ mm}$ while the length of the head of the connection tools is $L_1 = 15 \text{ mm}$, and the thickness of the nut is $m = 13 \text{ mm}$. The outer diameter of the hexagon socket is now compared to the mean pitch of the screws from **equation 24**.

$$D_2 = 32 \text{ mm} < t_B = 40.25 \text{ mm}$$

Equation 61. Comparison between the mean pitch of the screws and the outer diameter.

The outer diameter of the hexagon socket D_2 is smaller than the mean screw pitch diameter t_B so the number of screws $n_{screws} = 16 \text{ screws}$ and the diameter of the pitch circle diameter of the end plate $C_{HD} = 205 \text{ mm}$ is acceptable for the design.

7.2. Milling tools

The guiding angle at the water inlet and outlet is featured in the new CO₂ electrolyzer design. This angle is used to link the inlet and outlet with the flow channels of the flow field. The selection of the milling tools is decided to enable the manufacturing of the guiding angle. The entrance and exit of water in the flow field are determined as slots and pockets. According to Mikron Tools, a milling cutter CrazyMill Cool P&S Corner radius Z3 type A is selected [44]. This type of milling cutter is known as a milling cutter for slots and pockets in small spaces. This milling cutter can also be used to mill the titanium material workpiece German University



Figure 15. Diameter of the milling cutter.

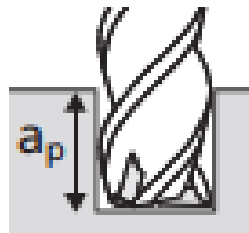


Figure 16. The depth of the milling cutter for one cut.

d_1 is known as the diameter of the milling cutter while a_p is known as the depth for one cut. The depth for one cut is calculated based on the material of the workpiece and the diameter of the cutter. Assumed the diameter of the milling cutter is $d_1 = 2 \text{ mm}$.

$d_1 = 2 \text{ mm}$			
$v_c \text{ (m min}^{-1}\text{)}$	$f_{z,p} \text{ (mm)}$	$f_{z,s} \text{ (mm)}$	$a_p \text{ (mm)}$
100	0.0018	0.0063	$0.25 \cdot d_1$

Table 4. The technical data when using slot milling cutter for titanium workpieces [44].

According to the velocity of the milling cutter is $v_c = 100 \text{ m min}^{-1}$. The feed per tooth for the slot milling is $f_{z,s} = 0.0063 \text{ mm}$, which means, the milling cutter has 16 teeth. The depth for one cut is:

$$a_p = 0.25 \cdot d_1 = 0.25 \cdot 2 = 0.5 \text{ mm}.$$

Equation 62. Depth of the cut.



8. 3D CAD models of reactor component

This chapter will show the CAD models design of the zero-gap electrolyzer which is based on the calculations and selections in **Chapter 4 and Chapter 5**, and drafted by Autodesk Inventor 2022 software.

8.1. Anode flow field

Figure 17 and 18 illustrate the overview design with the front and back view of the anode flow field. From **figure 18**, the centering method is changed when screws are replaced by 2 pins. The inlets and outlets of water have the guiding angle in the new design.

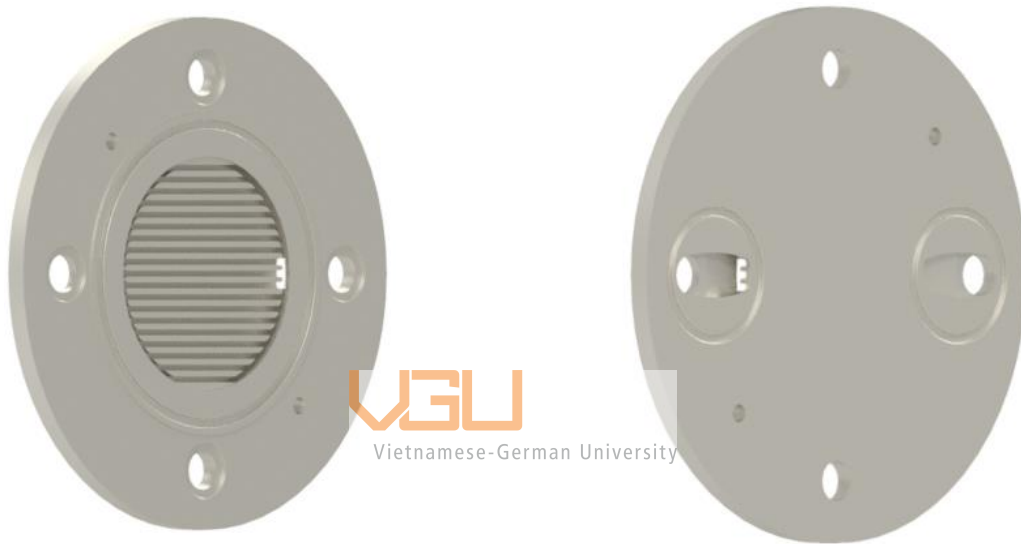


Figure 17. Front view of anode flow field design. **Figure 18. Back view of the anode flow field design.** **Figure 19** shows the overview dimensions of the new anode design, which include the **cross-section A-A and A-B**. The diameter of the electrodes is increased to $d_{electrode} = 80 \text{ mm}$. The outer diameter of the flow field is $d_{flow \text{ field}} = 180 \text{ mm}$, while the diameter of the inlets and outlets is $d_{inlets/outlets} = 13 \text{ mm}$. In addition, according to the calculations in **chapter 5 section 3**, the minimum area for the water flow to keep laminar flow condition is $A_{water} = 38.5 \text{ mm}^2$. The **cross-section A-A** shows the dimension of the water inlet with the height of the water inlet is $h_{water} = 4 \text{ mm}$ and the width of the water inlet is $w_{water} = 10 \text{ mm}$ to get the area of water flow is $A_{water} = 40 \text{ mm}^2$. Furthermore, the **cross-section A-B** illustrates the design of the flow channels. The fluid flow channels are 2 mm thin while the gaps between them are 2 mm , which according to the International Journal of Hydrogen Energy written by X. Li and I. Sabir when the width of the flow channels should be in the range of 1-2 mm [10].

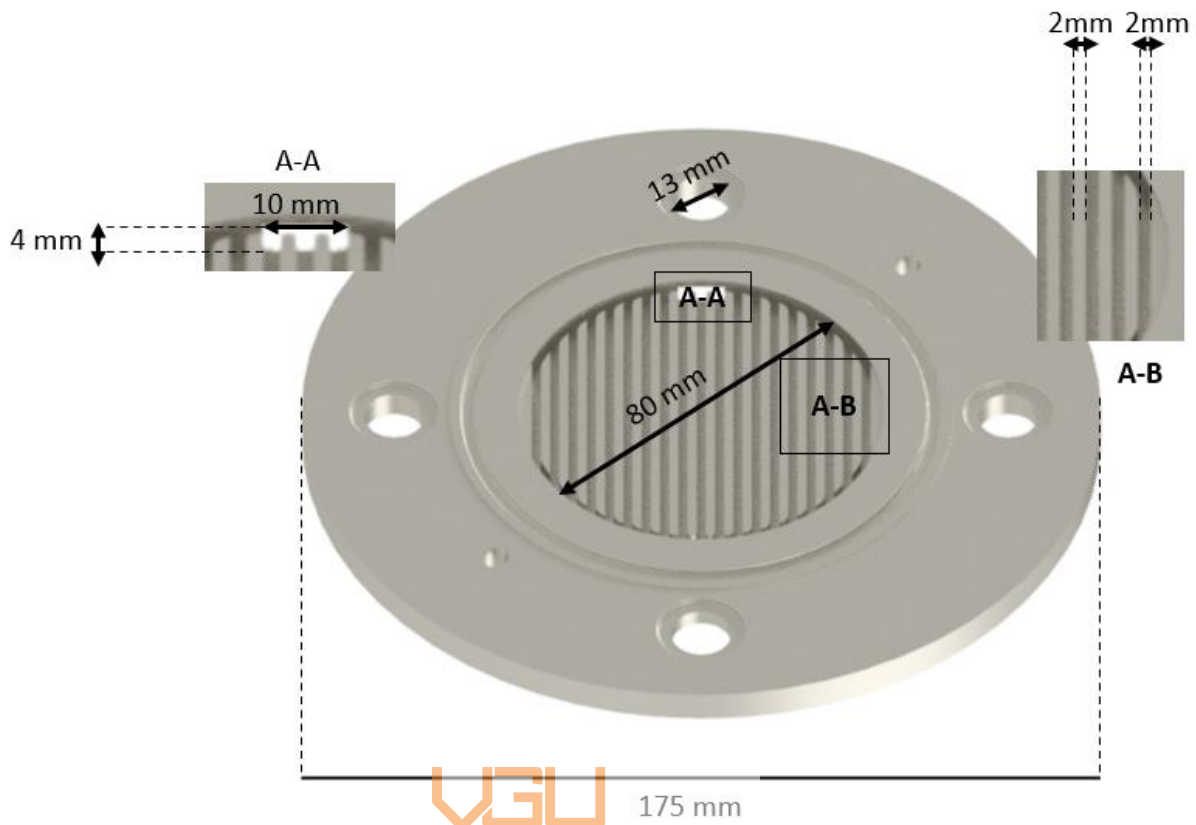


Figure 19. Dimensions of the anode flow field.

For the last anode flow field, the inlet and outlet of CO₂ are closed. In addition, this flow field contains the additional O-ring in order to reduce the stress between the copper plate and the flow field during the reaction.

8.2. Cathode flow field

Figure 20 and 21 illustrate the overview design with the front and back view of the anode flow field. From **figure 21**, the centering method is changed when screws are replaced by 2 pins. The inlets and outlets of water have the guiding angle in the new design.

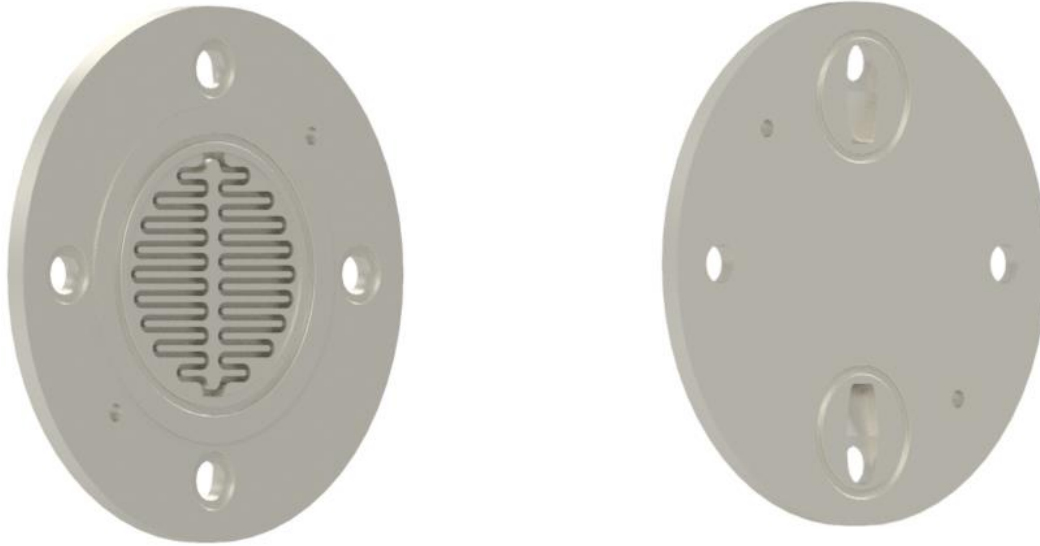


Figure 20. Front view of the cathode flow field design. Figure 21. Back view of the cathode flow field design. Figure 22 shows the new diameter of electrodes at the cathode flow fields is doubled to $d_{electrode} = 80\text{ mm}$. In addition, the height and the width of the water inlet and outlet of the cathode flow field are shown in **cross-section A-A of figure 22**. These parameters create the $A_{water} = 40\text{ mm}^2$ area of water flow in the cathode flow field.

For the last cathode flow field, the inlet and outlet of CO_2 are closed. In addition, this flow field contains the additional O-ring in order to reduce the stress between the copper plate and the flow field during the reaction.

Vietnamese-German University

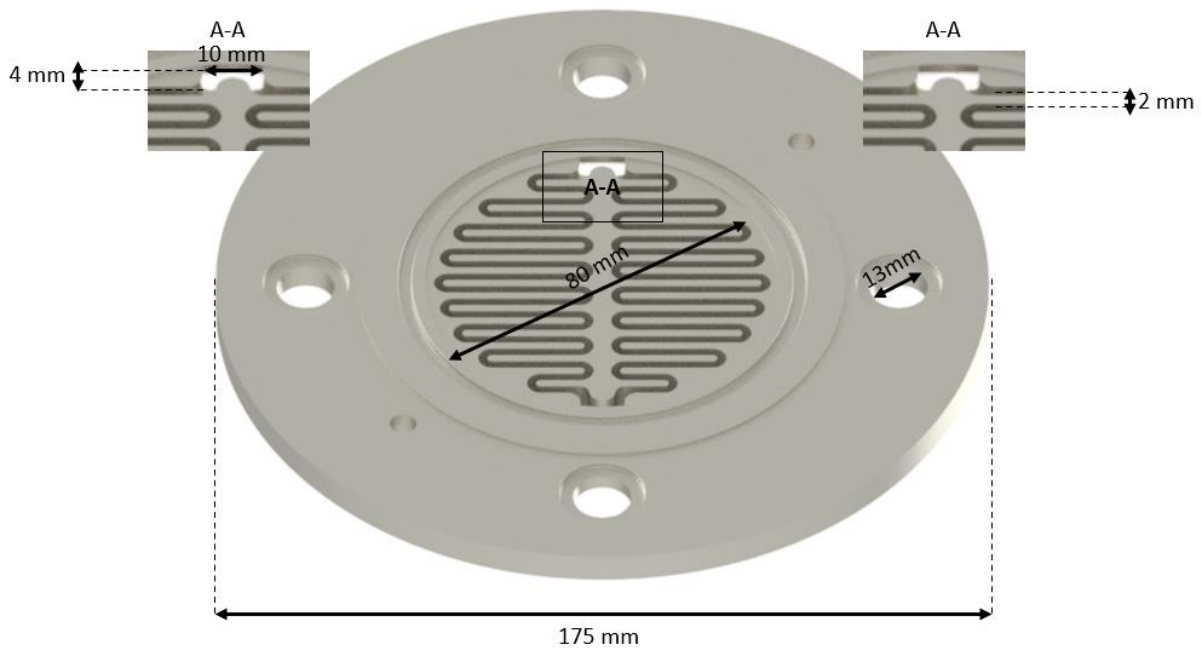


Figure 22. Dimension of the cathode flow field.

8.3. End plate

The end plate designs are shown in **figure 23** and **figure 24**. The end plates include the pins to centering stacks, which are shown in **figure 25**, and the screw holes to centering the end plates and insulations. There are CO₂ and water inlet and outlet for both end plates. The screws pitch for the CO₂ and water inlet and outlets at both inlets are the type of NPT 3/4.

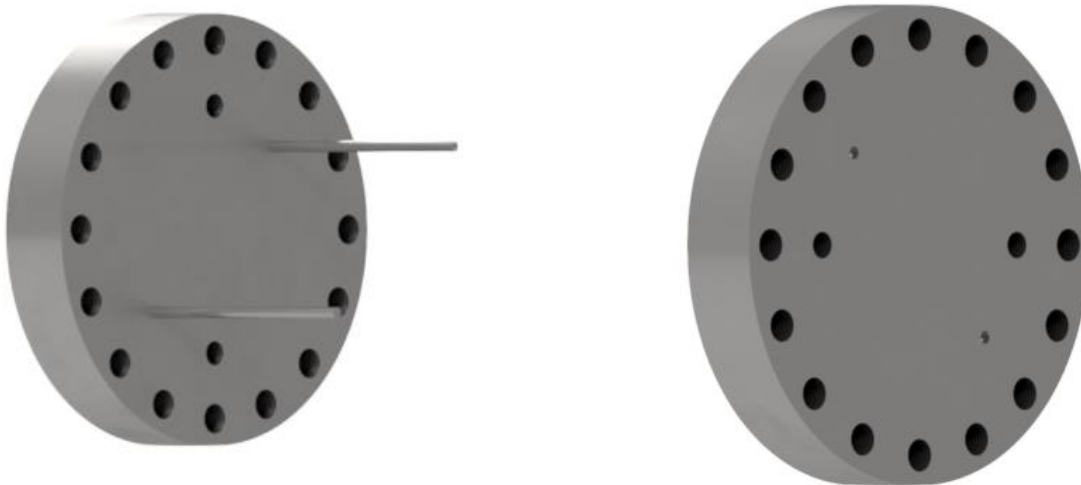


Figure 23. End plate at the last cathode flow field side. **Figure 24.** End plate at the last anode flow field side.

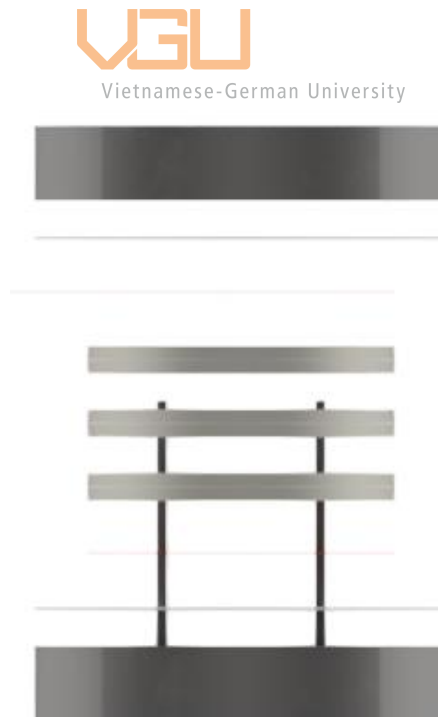


Figure 25. Pin centering.

8.4. Overview

Figures 26, and 27 show an overview of the exploded view of each stack, which includes the O-ring, one gas diffusion layer, one membrane, two electrodes, one anode, and one cathode flow field. The last stacks, which are attached to the copper plates, have two different flow fields.

Figure 27 illustrates the last stack with a different cathode flow field.

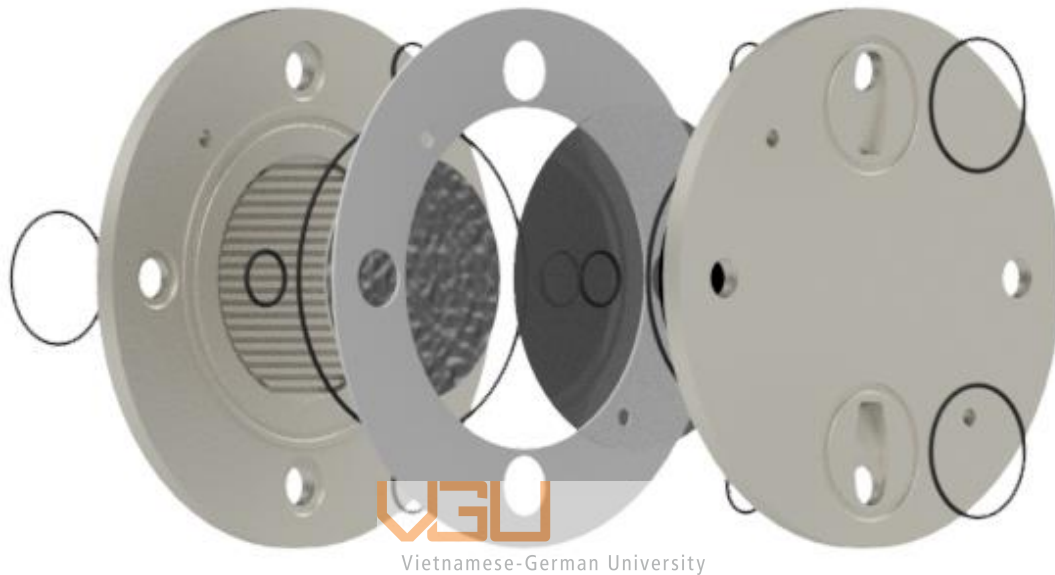


Figure 26. Exploded view of one stack.

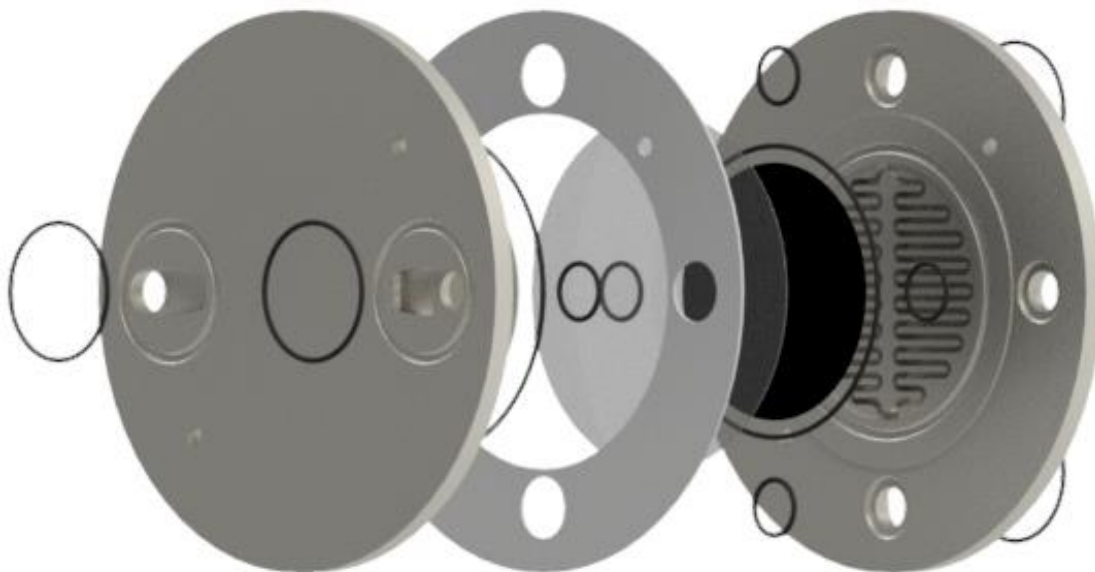


Figure 27. The last stack with different anode flow field.

Figure 28 shows the cell assembly design including 8 stacks, 2 end plates, 2 copper plates, 2 insulations, screws, washers, and nuts. **Figure 29** illustrates the exploded view of the cell assembly with 3 stacks, 2 copper plates, 2 insulations, 2 end plates, screws, washers, and nuts.



Figure 28. The cell assembly design.
Vietnamese-German University



Figure 29. Exploded view of the cell assembly.

9. Conclusion and outlook

Overall, the scaled-up design of the zero-gap electrolyzer has been proven to work under the high pressurization of the continuous electrolysis of CO₂ to CO according to the calculations in chapter IV, and V. In addition, the extension parameters were also noticed in chapter VI in order to prove the suitability of the design in manufacturing.


Since the structure of the original electrolyzer is working well, the idea for the structure of the new design is taken from the original one. However, the sizes of the components are recalculated to be suitable in order to meet the requirements of the new design, which also answers the question in **chapter 4**. The diameter of the electrodes in the new design is $d_{electrodes} = 80 \text{ mm}$, which leads to the change in the diameter of the other components. The diameter of the flow fields is $d_{flow \text{ field}} = 180 \text{ mm}$, and the diameter of the end plate is $d_{endplate} = 280 \text{ mm}$. In addition, the diameter of the fluid and gas inlets and outlets are also recalculated in order to keep the status of the flow laminar during the reaction. The widths and the gaps of the flow channels are 2 mm, which allows the milling cutter chosen in chapter VI to manufacture. Furthermore, the way to centering the components is also changed into the pins instead of using screws like the original design in order not to insulate the screws. The total mass of the new electrolyzer is about $m_{electrolyzer} = 26.5 \text{ kg}$.

According to the calculations and collected data, the requirements for the scale-up reactor have been solved. The larger the area of the electrodes, the more CO₂ is connected to CO during the process. In addition, the electrolyzer can be operated under 200 bars(g) even though there are changes in the structure in order to save the material. The new design has been sketched up and represents the positive outcomes when it is proved and calculated clearly by the norms and references from the former designs. However, further investigations need to be carried out to prove the stability of the design and put it into industrial-relevant applications.

For future research work, it is necessary to simulate the motion of the gas and water flow by CFD software in order to ensure the type of flow is stable. In addition, the way to place the new cell has to be thought out in order to prevent the reaction from being affected. These researches are included to demonstrate the long-term stability in use before developing the larger electrolyzer that is applied to the renewable energy industry.

References

- [1] IEA, international energy agency, “CO₂ Emissions in 2022,”.
- [2] B. Endródi, G. Bencsik, F. Darvas et al., “Continuous-flow electroreduction of carbon dioxide,” *Progress in Energy and Combustion Science*, vol. 62, pp. 133–154, 2017.
- [3] S. Liang, N. Altaf, L. Huang et al., “Electrolytic cell design for electrochemical CO₂ reduction,” *Journal of CO₂ Utilization*, vol. 35, pp. 90–105, 2020.
- [4] “WO2020240218A1,”.
- [5] S. Hernandez-Aldave and E. Andreoli, “Fundamentals of Gas Diffusion Electrodes and Electrolysers for Carbon Dioxide Utilisation: Challenges and Opportunities,” *Catalysts*, vol. 10, no. 6, p. 713, 2020.
- [6] Eduardo Alberto García Alanís, *Investigation of cathode-side pressure in the continuous electrolysis of CO₂ to syngas in a zero-gap electrolyzer*, Bachelor thesis, 2023.
- [7] O. Evers, “Electrochemical reduction of CO₂ under supercritical conditions,”.
- [8] S. Heuser, *Construction and optimization of a continuous test stand for the electrochemical reduction of compressed carbon dioxide in a differential pressure cell*, Mater thesis, 2021.
- [9] D. S. Falcão and A. Pinto, “A review on PEM electrolyzer modelling: Guidelines for beginners,” *Journal of Cleaner Production*, vol. 261, p. 121184, 2020.
- [10] X. LI and I. SABIR, “Review of bipolar plates in PEM fuel cells: Flow-field designs,” *International Journal of Hydrogen Energy*, vol. 30, no. 4, pp. 359–371, 2005.
- [11] M. S. Sajna, S. Zavahir, A. Popelka et al., “Electrochemical system design for CO₂ conversion: A comprehensive review,” *Journal of Environmental Chemical Engineering*, vol. 11, no. 5, p. 110467, 2023.
- [12] Wikipedia, “Membrane electrode assembly.”
https://en.wikipedia.org/wiki/Membrane_electrode_assembly.
- [13] Ö. F. Selamat, M. C. Acar, M. D. Mat et al., “Effects of operating parameters on the performance of a high-pressure proton exchange membrane electrolyzer,” *International Journal of Energy Research*, vol. 37, no. 5, pp. 457–467, 2013.
- [14] Y. Yang and F. Li, “Reactor design for electrochemical CO₂ conversion toward large-scale applications,” *Current Opinion in Green and Sustainable Chemistry*, vol. 27, p. 100419, 2021.
- [15] M. Goldman, E. W. Lees, P. L. Prieto et al., “Chapter 10. Electrochemical Reactors,” in *Carbon Dioxide Electrochemistry*, M. Robert, C. Costentin, and K. Daasbjerg, Eds., pp. 408–432, Royal Society of Chemistry, Cambridge, 2020.
- [16] “Schematic composition of a gas diffusion electrode (GDE) and the three-phase interface,”
https://www.researchgate.net/figure/Schematic-composition-of-a-gas-diffusion-electrode-GDE-and-the-three-phase-interface_fig4_317580649.
- [17] D. Wakerley, S. Lamaison, J. Wicks et al., “Gas diffusion electrodes, reactor designs and key metrics of low-temperature CO₂ electrolysers,” *Nature Energy*, vol. 7, no. 2, pp. 130–143, 2022.
- [18] D. M. Weekes, D. A. Salvatore, A. Reyes et al., “Electrolytic CO₂ Reduction in a Flow Cell,” *Accounts of chemical research*, vol. 51, no. 4, pp. 910–918, 2018.
- [19] H. Kahraman and M. F. Orhan, “Flow field bipolar plates in a proton exchange membrane fuel cell: Analysis & modeling,” *Energy Conversion and Management*, vol. 133, pp. 363–384, 2017.
- [20] L. Yuan, S. Zeng, X. Zhang et al., “Advances and challenges of electrolyzers for large-scale CO₂ electroreduction,” *Materials Reports: Energy*, vol. 3, no. 1, p. 100177, 2023.
- [21] G. Yang, J. Mo, Z. Kang et al., “Additive manufactured bipolar plate for high-efficiency hydrogen production in proton exchange membrane electrolyzer cells,” *International Journal of Hydrogen Energy*, vol. 42, no. 21, pp. 14734–14740, 2017.

- [22] L. Hoof, N. Thissen, K. Pellumbi et al., “Hidden parameters for electrochemical carbon dioxide reduction in zero-gap electrolyzers,” *Cell Reports Physical Science*, vol. 3, no. 4, p. 100825, 2022.
- [23] Dr. Colleen Spiegel, “Membrane Properties and Characterization for Zero-Gap CO₂ Electrolyzers,” <https://www.fuelcellstore.com/blog-section/membrane-properties-characterization-zero-gap-co2-electrolyzer#:~:text=These%20electrolyzers%20are%20called%20%E2%80%9Czero,are%20pressed%20or%20bonded%20together.>
- [24] Charles Delacourt, Paul L. Ridgway, John B. Kerr,* and John Newman*, “Design of an Electrochemical Cell Making Syngas (CO + H₂) from CO₂ and H₂O Reduction at Room Temperature,” 2008.
- [25] Dennis Blaudszun, *Development of novel membrane electrode units for the electrochemical conversion of CO₂ to CO*, Master thesis, 2022.
- [26] Technischen Überwachungs-Vereine, *AD2000*, Essen, 2000.
- [27] DIN-Normenausschuss Nichteisenmetalle (FNNE), *DIN EN 13445-3*, DEUTSCHE NORM, Germany, 2003.
- [28] DIN-Normenausschuss Nichteisenmetalle, “DIN EN 13445-11,” 2018.
- [29] DIN-Normenausschuss Nichteisenmetalle, “DIN EN 13445-12,” 2019.
- [30] H. Wittel, C. Spura, and D. Jannasch, *Roloff-Matek*, Springer Fachmedien Wiesbaden, Wiesbaden, 2021.
- [31] “JIS B0401-1,-2,” 1998.
- [32] Ganternorm, “GN 6339,”.
- [33] Technischen Überwachungs-Vereine, *AD2000 B8*, Essen, 2000.
- [34] DIN-Normenausschuss Nichteisenmetalle (FNNE), *DIN EN 10088-3*, DEUTSCHE NORM, Germany, 1995.
- [35] DIN-Normenausschuss Nichteisenmetalle, “DIN 17861 - Nahtlose kreisförmige Rohre aus Titan und Titanlegierungen,”

- [36] DIN-Normenausschuss Nichteisenmetalle, “DIN EN 12449, Kupfer und Kupferlegierungen – Nahtlose Rundrohre zur allgemeinen Verwendung; Deutsche Fassung EN 12449:2023,”.
- [37] H. Wittel, C. Spura, and D. Jannasch, *Roloff/Matek Maschinenelemente Formelsammlung*, Springer Fachmedien Wiesbaden, Wiesbaden, 2021.
- [38] DIN-Normenausschuss Nichteisenmetalle, “DIN ISO 3601-2,”.
- [39] Bronkhorst, “CO₂ properties,” <https://www.bronkhorst.com/de-de/>.
- [40] National Institute of Standards and Technology, “Properties of CO₂ and water,” <https://www.nist.gov/>.
- [41] T. L. Bergman and A. S. Lavine, *Fundamentals of heat and mass transfer*, John Wiley & Sons, Hoboken, NJ, 2017.
- [42] Wegertseder GmbH, “DIN 934,” www.schrauben-shop.de.
- [43] MiSUMi, “Hex socket,” <https://uk.misumi-ec.com/vona2/detail/223000327504/?HissuCode=3S-23>.
- [44] Mikron Tool, “MikronTool_Cutting data_CMC-P&S_TypeA-Keyways_Plunge_Slot_ENG,” <https://www.mikrontool.com/en/Products/CrazyMill-Cool-P-S/Description>.
- [45] DIN-Normenausschuss Nichteisenmetalle, “DIN 7093-1,” 2000.

Appendix

Size	Diameter of washers
M6	18
M8	24
M10	30
M12	37
M16	50

Table 1. Diameter of the washer [45].

	M12	M16
Class	12.9	12.9
Head type	Socket head	Socket head
A_s	115 mm ²	157 mm ²
A_p	90 mm ²	181 mm ²
F_{sp}	72.1 kN	135 kN
M_{sp}	160 Nm	395 Nm
d₃	9.853 mm	13.546 mm
μ_G=μ_k	0.14	0.14

Table 2. Properties of the M12 and M16 screws [30].

d_2	b_4		h
	Installation width for liquid	Installation width for gas or vacuum	
	+0.2 0		
1.78	3.2	2.9	1.3
2.62	4.0	3.6	2
3.53	5.3	4.8	2.7
5.33	7.6	7	4.2
6.99	9	8.5	5.7

Table 3. Detailed dimensions of O-ring installation space in fluid and gas applications [38].

Pressure (bar)	ρ at 25 ^o C (kg m ⁻³)	ρ at 40 ^o C (kg m ⁻³)	ρ at 60 ^o C (kg m ⁻³)
0	1.8	1.7	1.6
10	20.8	19.6	18.2
20	42.2	39.3	36.1
30	67.1	61.4	55.6
40	97.4	86.8	77.1
50	137.5	117.1	101
60	307.3	155	128.2
70	717.7	207.5	159.6
80	739.3	299.6	197.1
90	765.2	499.9	240.9
100	784.8	631.7	300.1
110	801.8	662.1	367
120	817.3	692.4	421.8
130	831.3	722.7	484.6
140	844.2	753	552.4
150	855.9	781.5	596.7
160	866.6	793.4	630.3
170	876.5	805.3	654.3
180	885.6	817.3	678.2
190	893.9	829.2	702.2
200	901.7	840.7	725.1

Table 4. CO₂ density found from the NIST website [40].

Pressure (bar)	$\mu \cdot 10^{-7}$ at 25°C (Pa.s)	$\mu \cdot 10^{-7}$ at 40°C (Pa.s)	$\mu \cdot 10^{-7}$ at 60°C (Pa.s)
0	149.05	156.19	165.62
10	150.18	157.44	166.97
20	151.91	159.19	168.72
30	154.55	161.64	171
40	158.66	165.09	173.95
50	165.58	170.1	177.82
60	180.22	177.76	182.96
70	620.63	190.76	189.92
80	674.44	219.27	199.64
90	714.4	341.78	213.76
100	747.6	476.52	235.17
110	776.63	542.49	268.15
120	802.8	588.61	314.67
130	826.85	625.47	367.44
140	849.27	656.86	416.49
150	870.29	684.61	458.81
160	890.43	709.72	495.18
170	909.58	732.82	526.98
180	927.97	754.35	555.32
190	945.7	774.6	580.98
200	962.85	793.79	604.51

Table 5. Dynamic viscosity of CO₂ found from the NIST website [40].

Pressure (bar)	v at 25 ⁰ C (mm s ⁻¹)	v at 40 ⁰ C (mm s ⁻¹)	v at 60 ⁰ C (mm s ⁻¹)
0	1630.15	1713.55	1823.83
10	141.97	150.60	161.94
20	69.86	75.03	81.62
30	43.92	47.99	53
40	30.26	33.94	38.24
50	21.44	25.17	29.18
60	9.59	19.01	22.99
70	4.11	14.2	18.47
80	3.99	9.84	14.95
90	3.85	5.9	12.24
100	3.76	4.67	9.82
110	3.68	4.45	8.03
120	3.61	4.26	6.99
130	3.55	4.08	6.08
140	3.49	3.91	5.34
150	3.44	3.77	4.94
160	3.40	3.71	4.68
170	3.36	3.66	4.5
180	3.33	3.61	4.35
190	3.30	3.55	4.2
200	3.27	3.51	4.06

Table 6. Velocity of the CO₂ at the inlet and outlet of the flow fields.

Pressure (bar)	25 °C	Flow type	40 °C	Flow type	60 °C	Flow type
0	2372.87924	mix	2264.4065	laminar	2135.477	laminar
10	2355.02498	mix	2246.42817	laminar	2118.211	laminar
20	2328.2052	mix	2221.73284	laminar	2096.24	laminar
30	2288.43514	laminar	2188.05773	laminar	2068.29	laminar
40	2229.15449	laminar	2142.33237	laminar	2033.214	laminar
50	2135.99258	laminar	2079.23369	laminar	1988.964	laminar
60	1962.47726	laminar	1989.63575	laminar	1933.087	laminar
70	569.868765	laminar	1854.04514	laminar	1862.245	laminar
80	524.40195	laminar	1612.97784	laminar	1771.577	laminar
90	495.069501	laminar	1034.81085	laminar	1654.555	laminar
100	473.084071	laminar	742.209459	laminar	1503.923	laminar
110	455.40045	laminar	651.952389	laminar	1318.955	laminar
120	440.555121	laminar	600.869254	laminar	1123.964	laminar
130	427.741007	laminar	565.459017	laminar	962.5453	laminar
140	416.449011	laminar	538.436884	laminar	849.1864	laminar
150	406.343882	laminar	516.611869	laminar	770.8586	laminar
160	397.198714	laminar	498.334063	laminar	714.2406	laminar
170	388.836223	laminar	482.625544	laminar	671.1406	laminar
180	381.13048	laminar	468.850867	laminar	636.8898	laminar
190	373.985039	laminar	456.593921	laminar	608.7605	laminar
200	367.323728	laminar	445.55569	laminar	585.065	laminar

Table 7. Reynolds number and type of CO₂ flow condition with $d_{inlet/outlet} = 12 \text{ mm}$.

Pressure (bar)	25 °C	Flow type	40 °C	Flow type	60 °C	Flow type
0	2190.35007	laminar	2090.22139	laminar	1971.209	laminar
10	2173.86921	laminar	2073.626	laminar	1955.271	laminar
20	2149.11249	laminar	2050.83032	laminar	1934.991	laminar
30	2112.40167	laminar	2019.7456	laminar	1909.191	laminar
40	2057.68107	laminar	1977.53757	laminar	1876.813	laminar
50	1971.68546	laminar	1919.29264	laminar	1835.967	laminar
60	1811.51747	laminar	1836.58685	laminar	1784.388	laminar
70	526.032706	laminar	1711.42629	laminar	1718.996	laminar
80	484.063339	laminar	1488.90262	laminar	1635.302	laminar
90	456.987231	laminar	955.210013	laminar	1527.281	laminar
100	436.692988	laminar	685.116424	laminar	1388.237	laminar
110	420.369646	laminar	601.802205	laminar	1217.496	laminar
120	406.666266	laminar	554.648542	laminar	1037.505	laminar
130	394.837852	laminar	521.962169	laminar	888.5034	laminar
140	384.414471	laminar	497.018662	laminar	783.8644	laminar
150	375.08666	laminar	476.872494	laminar	711.5618	laminar
160	366.644967	laminar	460.000674	laminar	659.299	laminar
170	358.925744	laminar	445.500502	laminar	619.5144	laminar
180	351.812751	laminar	432.785415	laminar	587.8983	laminar
190	345.216959	laminar	421.471312	laminar	561.9327	laminar
200	339.068056	laminar	411.282176	laminar	540.06	laminar

Table 8. Reynolds number and type of CO₂ flow condition with $d_{inlet/outlet} = 13mm$.

Pressure (bar)	ρ at 25 ⁰ C (kg m ⁻³)	ρ at 40 ⁰ C (kg m ⁻³)	ρ at 60 ⁰ C (kg m ⁻³)
0	997	992.18	983.16
10	997.45	992.61	983.59
20	997.9	993.05	984.02
30	998.35	993.48	984.46
40	998.8	993.92	984.89
50	999.25	994.36	985.33
60	999.69	994.79	985.76
70	1000.1	995.22	986.19
80	1000.6	995.65	986.62
90	1001	996.08	987.05
100	1001.5	996.52	987.48
110	1001.9	996.94	987.9
120	1002.3	997.37	988.33
130	1002.8	997.8	988.76
140	1003.2	998.23	989.18
150	1003.7	998.65	989.6
160	1004.1	999.08	990.03
170	1004.5	999.5	990.45
180	1005	999.92	990.87
190	1005.4	1000.3	991.29
200	1005.8	1000.8	991.71

Table 9. Water density found from the NIST [40].

Pressure (bar)	$\mu \cdot 10^{-6}$ at 25°C (Pa.s)	$\mu \cdot 10^{-6}$ at 40°C (Pa.s)	$\mu \cdot 10^{-6}$ at 60°C (Pa.s)
0	890.04	652.72	466.02
10	889.9	652.84	466.25
20	889.76	652.97	466.49
30	889.63	653.1	466.73
40	889.5	653.23	466.97
50	889.38	653.36	467.22
60	889.26	653.49	467.46
70	889.14	653.62	467.7
80	889.03	653.76	467.94
90	888.92	653.89	468.19
100	888.81	654.03	468.43
110	888.7	654.17	468.67
120	888.6	654.31	468.91
130	888.5	654.45	469.16
140	888.41	654.59	469.4
150	888.32	654.74	469.65
160	888.23	654.88	469.89
170	888.15	655.03	470.14
180	888.07	655.18	470.38
190	887.99	655.32	470.63
200	887.91	655.47	470.87

Table 10. Dynamic viscosity of water found from the NIST [40].

Pressure (bar)	25 °C	Flow type	40 °C	Flow type	60 °C	Flow type
0	1238.064505	laminar	1680.046	laminar	2331.725	mix
10	1238.818172	laminar	1680.465	laminar	2331.594	mix
20	1239.572076	laminar	1680.875	laminar	2331.413	mix
30	1240.312276	laminar	1681.269	laminar	2331.256	mix
40	1241.052692	laminar	1681.678	laminar	2331.076	mix
50	1241.779361	laminar	1682.088	laminar	2330.869	mix
60	1242.493798	laminar	1682.481	laminar	2330.689	mix
70	1243.171137	laminar	1682.873	laminar	2330.509	mix
80	1243.946555	laminar	1683.24	laminar	2330.33	mix
90	1244.59783	laminar	1683.632	laminar	2330.101	mix
100	1245.373617	laminar	1684.015	laminar	2329.921	mix
110	1246.025229	laminar	1684.364	laminar	2329.719	mix
120	1246.662974	laminar	1684.73	laminar	2329.54	mix
130	1247.425256	laminar	1685.096	laminar	2329.311	mix
140	1248.049253	laminar	1685.462	laminar	2329.109	mix
150	1248.797796	laminar	1685.785	laminar	2328.858	mix
160	1249.422059	laminar	1686.15	laminar	2328.68	mix
170	1250.032373	laminar	1686.472	laminar	2328.429	mix
180	1250.767252	laminar	1686.795	laminar	2328.228	mix
190	1251.377798	laminar	1687.075	laminar	2327.977	mix
200	1251.988454	laminar	1687.532	laminar	2327.777	mix

Table 11. Reynolds number and type of flow condition of water with $d_{water} = 6 \text{ mm}$.

Pressure (bar)	25 °C	Flow type	40 °C	Flow type	60 °C	Flow type
0	1061.198147	laminar	1440.039	laminar	1998.621	laminar
10	1061.844148	laminar	1440.399	laminar	1998.509	laminar
20	1062.490351	laminar	1440.75	laminar	1998.354	laminar
30	1063.124808	laminar	1441.087	laminar	1998.22	laminar
40	1063.75945	laminar	1441.439	laminar	1998.065	laminar
50	1064.38231	laminar	1441.79	laminar	1997.888	laminar
60	1064.994684	laminar	1442.126	laminar	1997.734	laminar
70	1065.57526	laminar	1442.463	laminar	1997.58	laminar
80	1066.239904	laminar	1442.777	laminar	1997.426	laminar
90	1066.79814	laminar	1443.113	laminar	1997.229	laminar
100	1067.4631	laminar	1443.442	laminar	1997.075	laminar
110	1068.021625	laminar	1443.741	laminar	1996.902	laminar
120	1068.568263	laminar	1444.055	laminar	1996.748	laminar
130	1069.221648	laminar	1444.368	laminar	1996.553	laminar
140	1069.756503	laminar	1444.681	laminar	1996.379	laminar
150	1070.398111	laminar	1444.958	laminar	1996.164	laminar
160	1070.933193	laminar	1445.271	laminar	1996.011	laminar
170	1071.45632	laminar	1445.548	laminar	1995.796	laminar
180	1072.086216	laminar	1445.824	laminar	1995.624	laminar
190	1072.609541	laminar	1446.065	laminar	1995.409	laminar
200	1073.13296	laminar	1446.456	laminar	1995.237	laminar

Table 12. Reynolds number and type of flow condition of water with $d_{water} = 7 \text{ mm}$.

Pressure (bar)	25 °C	Flow type	40 °C	Flow type	60 °C	Flow type
0	571.4143871	laminar	775.4059	laminar	1076.181	laminar
10	571.7622334	laminar	775.5993	laminar	1076.12	laminar
20	572.1101891	laminar	775.7887	laminar	1076.037	laminar
30	572.4518196	laminar	775.9701	laminar	1075.964	laminar
40	572.79355	laminar	776.1593	laminar	1075.881	laminar
50	573.128936	laminar	776.3484	laminar	1075.786	laminar
60	573.4586762	laminar	776.5296	laminar	1075.703	laminar
70	573.7712939	laminar	776.7107	laminar	1075.62	laminar
80	574.1291793	laminar	776.8799	laminar	1075.537	laminar
90	574.4297677	laminar	777.0609	laminar	1075.431	laminar
100	574.7878231	laminar	777.2378	laminar	1075.348	laminar
110	575.0885674	laminar	777.3989	laminar	1075.255	laminar
120	575.382911	laminar	777.5678	laminar	1075.172	laminar
130	575.7347335	laminar	777.7367	laminar	1075.067	laminar
140	576.0227322	laminar	777.9054	laminar	1074.974	laminar
150	576.3682136	laminar	778.0544	laminar	1074.858	laminar
160	576.6563348	laminar	778.223	laminar	1074.775	laminar
170	576.9380184	laminar	778.3719	laminar	1074.66	laminar
180	577.2771933	laminar	778.5207	laminar	1074.567	laminar
190	577.5589836	laminar	778.6502	laminar	1074.451	laminar
200	577.8408247	laminar	778.8611	laminar	1074.358	laminar

Table 13. Reynolds number and type flow condition of water $d_{water} = 13 \text{ mm}$.

D	m	e	s
M8	6.5	14.4	13
M10	8	18.9	17
M12	10	21.1	19
M14	11	24.5	22
M16	13	26.8	24
M18	15	33	27
M20	16	35	30

Table 14. Technical data of hexagon nut [42].

Width of hexagon nuts (mm)	Dimensions (mm)			
	D_1	D_2	L_1	L
s				
22	23.5	30.0	14	33
23	25.5	31.0	14	33
24	25.5	32.0	15	34

Table 15. Technical data of the hexagon socket [43].

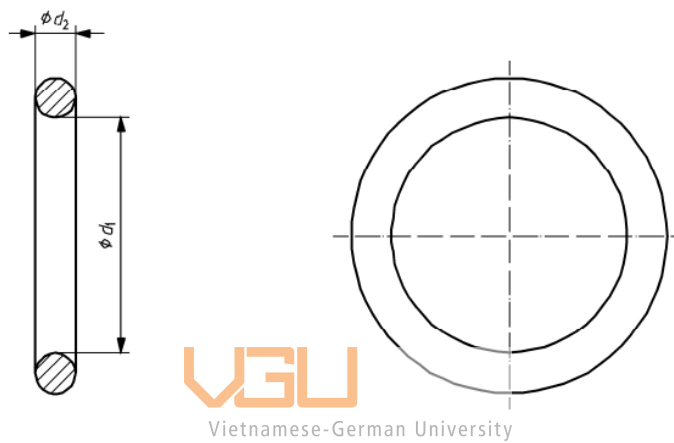


Figure 1. Typical O-ring design [38].

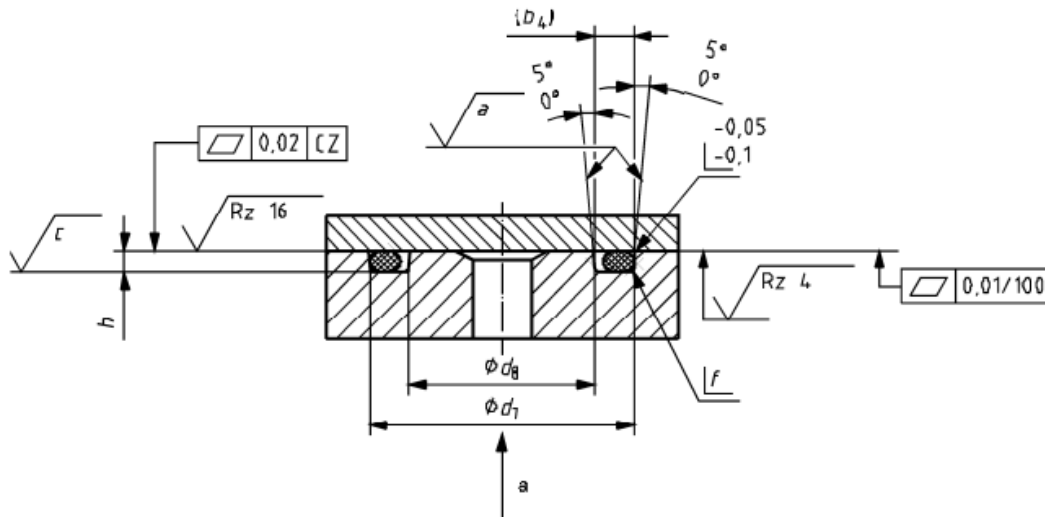


Figure 2. Cross-section of the sealing covered by 2 walls [38].

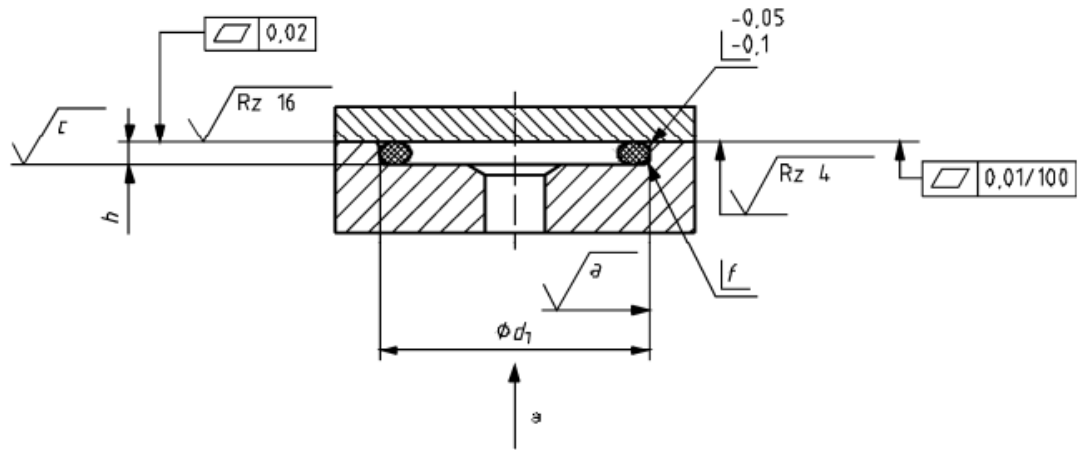


Figure 3. Cross-section of the sealing without wall [38].

Assurance

I hereby declare that I have written this thesis independently and have not used any sources or aids other than those stated aids or sources.

Oberhausen, 10/11/2023

Place, Date

Nguyen
Ngô Thanh Nguyễn

Signature



Vietnamese-German University